Neutron-fragment coincidence measurements in ^{14}N + Ho and ^{14}N + Ni reactions at 35 MeV/nucleon

B. A. Remington,* G. Caskey,† A. Galonsky, C. K. Gelbke, L. Heilbronn, J. Heltsley, and M. B. Tsang
National Superconducting Cyclotron Laboratory and Department of Physics and Astronomy, Michigan State University, East Lansing, Michigan 48824

F. Deak and A. Kiss
Department of Atomic Physics, Eötvös University, Budapest, Hungary H-1088

Z. Seres
Hungarian Academy of Sciences, Central Research Institute for Physics, Budapest 114, Hungary H-1525

J. Kasagi
Department of Physics, Tokyo Institute of Technology, O-Okayama, Meguro-Ku, Tokyo, Japan

J. J. Kolata
Nuclear Structure Laboratory and Department of Physics, University of Notre Dame, South Bend, Indiana 46556
(Received 31 March 1986)

We have studied $^{14}N+^{165}Ho$ and $^{14}N+Ni$ collisions at 35 MeV/nucleon by detecting neutrons at ten angles from 10° to 160° in coincidence with light fragments at six angles between 7° and 30°. For a given fragment, the seven spectra of coincident neutrons whose angles are not near the fragment angle were fitted with two moving, thermal sources. One source is a slowly-moving, targetlike source; the other is a faster (approximately half-beam-velocity), hotter source. The latter source, an intermediate-rapidity source, reproduces a left-right asymmetry in which the fragment-neutron cross sections are larger for emission to opposite sides of the beam axis than for emission to the same side. The temperature of the targetlike source is about 3.5 MeV with the Ni target and about 2.5 MeV with the Ho target. The corresponding values for the intermediate-rapidity source are 10 and 8.5 MeV. These source temperatures are approximately independent of fragment angle, but the measured neutron multiplicities increase with fragment angle. For the targetlike source the largest multiplicities, 1.6 for Ni and 9 for Ho, are about $\frac{3}{4}$ the values computed with a statistical code. The multiplicities of the intermediate-rapidity source are about $\frac{1}{4}$ the multiplicities of the targetlike source. The necessity for an intermediate-rapidity source is also demonstrated in terms of "missing momentum" in the final state of an assumed two-body, $^{14}N+$target inelastic collision. The mass number of this source is estimated in peripheral collisions and in central collisions. The approximate independence of source parameters on fragment angle may indicate that the neutrons and the fragments are emitted at different times during the reaction. The neutron multiplicities of the two sources have a parallel upward trend with fragment angle, indicating that the two sources may be correlated. We speculate that a small, hot source evolves into the cooler, large targetlike source.

I. INTRODUCTION

In concert with developments in heavy-ion accelerator technology, heavy-ion nuclear reactions have largely been studied at low energies ($E_{\text{beam}} \leq 10$ MeV/nucleon) and at high energies ($E_{\text{beam}} \geq 100$ MeV/nucleon). The low energy regime corresponds to beam energies per nucleon lower than either the speed of sound in nuclear matter (equivalent to about 15 MeV/nucleon) or the mean Fermi energy of nucleons in a nucleus (about 28 MeV).[1] The time scale of the interaction is hence large compared to the nuclear relaxation time. As a result, low energy nuclear collisions have been successfully described by equilibrium theories, as in the statistical model,[2] and by theories incorporating mean-field phenomena, such as the time-dependent Hartree-Fock (TDHF) approach.[3] On the other hand, high energy collisions occur on a time scale which is short compared to the nuclear relaxation time. Successful theories for the high energy regime typically divide the colliding nuclei into participant and spectator zones, as in the fireball model,[4] or assume the reactions to consist of a series of free nucleon-nucleon collisions, as in the intranuclear cascade model.[5]

With the advent of intermediate energy heavy-ion ac-

celerators, data are now emerging in the transition region (10 MeV/nucleon $\leq E_{\text{beam}} \leq$ 100 MeV/nucleon). The simplifying assumptions of interaction time being either long or short compared to the nuclear relaxation time no longer apply. Much theoretical activity is taking place to extend current high energy and low energy theories into the transition region;[6,7] additional approaches involve Fermi-jet[8,9] and hot-spot[10,11] models. Incumbent upon the experimental community is the task of producing data that can cleanly distinguish between currently emerging models, and establish clear landmarks and systematics by which the theorists can be guided.

One such landmark of the intermediate energy regime is the onset of preequilibrium particle emission. As beam energies exceed the "threshold" of $(E_{\text{c.m.}} - V_c)/\mu \approx 8$ MeV/nucleon, a distinct nonequilibrium or preequilibrium component of particle emission appears. Although various models have been proposed to explain preequilibrium particle emission (exciton model,[12–14] Fermi-jet model,[8,9] hot-spot model,[10,11] piston model,[15] "tangential-friction" model,[16,17] Harp-Miller-Berne model[7,18]), no one single approach can yet explain the systematic behavior of preequilibrium particle spectra over a broad energy and angular range. One notable common denominator of all preequilibrium emission, though, is the success of a thermal parametrization.

It has been shown in inclusive measurements that a single, relatively hot, intermediate-rapidity source (IRS) can reproduce the energy and angular distributions of light particles[19,20] and of complex fragments[21–23] as long as the forward-most angles are excluded. Preequilibrium light particle spectra taken in coincidence with fission fragments[24–26] or with projectilelike fragments[27,28] have also been successfully parametrized with a hot IRS. Particularly "clean" information about the nuclear reaction may be obtained from the energy and angular distributions of emitted neutrons since they are not subject to Coulomb distortions. For this reason numerous studies of neutrons in coincidence with evaporation residues,[29–34] with fission fragments,[29–32,35–37] and with projectilelike fragments[17,29,30,32–34,36–41] have been reported. In all studies in which preequilibrium neutron emission was unambiguously established[17,29,30,32–34,37,39] the preequilibrium component of neutron spectra could be parametrized with a hot thermal source. The pervasive success of the moving source model in parametrizing preequilibrium particle emission leads one to consider whether the IRS carries more fundamental information about the reaction mechanism. Indeed, one cannot help but wonder if an understanding of this thermal appearance of preequilibrium spectra might not be the link between the participant-spectator thermal description (fireball) of high energies and the compound nucleus thermal (statistical) description of low energies. Until this question is answered with a suitable theory, experimental interest will remain keen in mapping out the systematics of the transitional energy region.

Of particular relevance to the present study is a recent experiment to study the $^{14}N + ^{165}Ho$ system at 35 MeV/nucleon.[38,42–44] In that work neutrons were detected in coincidence with projectilelike fragments near and beyond the grazing angle. Considerable evidence for preequilibrium neutron emission in coincidence with both quasielastic and strongly damped fragments was observed.[38] This preequilibrium component was parametrized in terms of a hot thermal source moving at about half the beam velocity. One interesting feature observed was that for very peripheral collisions, the preequilibrium neutron spectra showed a distinct asymmetry at middle angles. More high energy neutrons were observed on the side of the beam opposite to that of the detected projectilelike fragment. This asymmetry was reproduced within the thermal-source parametrization by requiring the hot source to move off axis towards the side of the beam opposite the detected projectilelike fragment. For reactions leading to strongly damped fragments no asymmetry was detected. Asymmetry effects in preequilibrium particle emission have been observed before in both charged-particle—projectilelike fragment coincidence studies[16] and in neutron-projectilelike fragment coincidence studies.[17,39] No systematic trend has yet emerged, and results often depend on the method of isolating the preequilibrium component.

Motivated by these results, we conducted an experiment using a 35 MeV/nucleon beam of ^{14}N provided by the K500 cyclotron at the National Superconducting Cyclotron Laboratory at Michigan State University. To try to understand the target dependence of preequilibrium neutron emission, we selected targets of Ho as a relatively large nucleus and Ni as a significantly smaller nucleus. If the observed asymmetry was due to a shadowing effect, then the size of the target nucleus might be a pertinent parameter. In the earlier neutron study[38] fragments were detected at two angles, 10° and 30°, with the above-mentioned neutron asymmetry observed only for coincident fragments at 10° (which is near the grazing angle) resulting from quasielastic interactions. To try to understand the dependence of the asymmetry on impact parameter, as reflected in the angle of the coincidence fragment, we placed an array of fragment telescopes both inside and outside the grazing angle (8°) for the $^{14}N + ^{165}Ho$ system and near the grazing angle (4°) for the $^{14}N + Ni$ system.

In this paper we present a systematic study of neutrons detected in coincidence with light fragments (LF) in ^{14}N-induced reactions on targets of Ho and Ni at 35 MeV/nucleon incident energy. An analysis of the data is given in terms of moving, thermal sources. The deduced parameters of the sources are examined for correlations offering insight into the reaction mechanism of these particular nuclei. Hopefully, such insights should apply to a wide range of collision partners and at other energies in the transition region. In the next section of this paper a description of the experimental details is given. Since neutrons were detected in coincidence with fragments, a short discussion of the fragment energy, angle, and Z distributions is given in Sec. III. The neutron spectra are discussed in Sec. IV, and the results from a moving source analysis are presented in Sec. V. Also contained in Sec. V are the results of a two-body calculation, the results of multiplicity calculations done with a statistical code, and a discussion of the "size" of the hot source. A summary of our results is given in Sec. VI.

II. EXPERIMENTAL SETUP

As a detailed description of the experimental setup can be found in Ref. 45, only the salient features will be mentioned here. The detector arrangement is shown in Fig. 1. The scattering chamber was made of steel and had a 3 mm wall thickness and a 0.91 m diameter. Ten neutron detectors[44,45] were placed in a horizontal plane around the outside of the chamber at angles of $\pm 10°$, $\pm 30°$, $\pm 70°$, $\pm 110°$, and $\pm 160°$ and at distances ranging from 1.14 m at $\pm 160°$ to 2.42 m at $\pm 10°$. Each detector consisted of 1 liter of NE213 liquid scintillator contained in a sealed glass cell about 12.7 cm in diameter by 7.6 cm thick. Each cell was preceded by a 6 mm thick NE102A proton veto paddle to eliminate events due to high energy protons that traveled through the chamber wall and into the neutron detector. The time resolution of the detectors was measured to be slightly less than 1 ns. This was determined by event-mode sorting of fragment–gamma-ray coincidence events with the flight time of the fragment corrected for and the neutron detector threshold set at the ^{60}Co Compton edge. Combining this with the flight path and detector thickness allowed energy resolutions which, for 5 and 50 MeV neutrons, varied from 14% and 20% at the back angles to 6% and 8% at the forward angles.

Six Si telescopes for fragment detection were placed inside the chamber at angles of 7°, 10°, 15°, 18°, and 23° in the horizontal plane and 15° out of this plane directly below the beam axis. The target-to-collimator distance was about 25 cm, and the collimator aperture was 12.7 mm. For the Ho target the collimator for the 7° telescope was at 30 cm, and it had a 4.0 mm aperture. In order to stop quasielastic lithium fragments, each of the four forward-most telescopes had a stopping detector which was a combination of a 5 mm and a 1 mm Li-drifted Si detector. For the two largest fragment angles (18° and 23°), the additional 1 mm detector was not required. All telescopes were cooled to about $-10\,°$C by circulating refrigerated liquid methanol. This reduced the leakage current, and hence the noise, resulting from radiation damage in the Si. To inhibit secondary electrons knocked out of the target by the beam from entering the Si detectors, rare-earth Co magnets were mounted in front of each telescope.

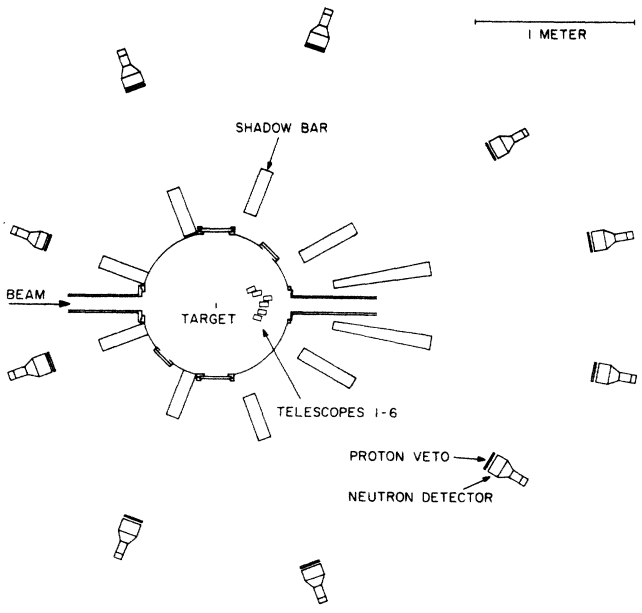

FIG. 1. Experimental setup. Ten neutron detectors, together with their proton veto detectors, are located around the chamber at symmetric angle pairs of $\pm 10°$, $\pm 30°$, $\pm 70°$, $\pm 110°$, and $\pm 160°$. Also shown are the positions of the shadow bars. Six triple-element Si telescopes were located inside the chamber at polar angles of 7°, 10°, 15°, 18°, and 23° in the horizontal plane, and at 15° directly below the beam direction.

The targets were 8.9 mg/cm^2 Ho, 4.6 mg/cm^2 Ni, 3.1 mg/cm^2 C, and 3.2 mg/cm^2 Mylar. A run with the carbon target gave us the data with which to subtract a possible contribution from ^{14}N + C reactions in case there was any appreciable carbon buildup on the Ni and Ho targets. Similarly, in case of oxidation of the targets, a short run with the Mylar target was conducted to determine the contribution from ^{14}N+O reactions. As was determined in a separate α-particle back-scattering experiment done on the tandem Van de Graaff system at the University of Notre Dame, the level of carbon buildup on our targets was $\leq 1\ \mu$g/cm^2 and the oxygen contamination was about 4 μg/cm^2. From our measurements taken with the carbon target, we determined that the contamination levels of neutrons produced from ^{14}N + C were negligible.

To reduce the level of background neutrons, the amount of material in the chamber and beamline near the target was kept low, and extensive shielding was installed around the beam dump. To determine the background contribution to our measured neutron spectra, periodically throughout the experiment data were taken with shadow bars placed as shown in Fig. 1. The background contribution was typically less than 10% of the total.

The time structure of the beam was not suitable for timing the neutrons against the cyclotron rf signal. Therefore neutrons were recorded in coincidence with and "timed against" a fragment in any one of the six Si telescopes, and the flight time of the fragment was added off-line to obtain the true neutron flight time. Neutron–gamma-ray discrimination was accomplished with commercially available pulse-shape discrimination modules,[46] using standard two-dimensional neutron–gamma-ray discrimination techniques.[47,48] For each event the following information was written onto magnetic tape: a neutron-fragment relative time signal; pulse-shape discrimination and light amplitude signals from the neutron detector; ΔE and E signals from the Si telescope; and a bit mask that recorded which combination of detectors fired. Downscaled fragment singles events were also recorded. The data were written onto tape with the aid of a CAMAC multiparameter data acquisition system incorporating an MC 68010 microprocessor, with typical acquisition rates of 800 events/s.[49] With the typical beam intensity of 2×10^{10}/s the live time was about 90%.

The thick Si detectors at angles $\theta \leq 15°$ were calibrated with the peak from elastically scattered beam particles.

For the telescopes at 18° and 23°, where we could not observe an elastic peak, the high energy calibration was transferred from the small-angle detectors with the aid of a charge-injection pulser. The ΔE detectors were calibrated with α-particle sources and the charge-injection pulser. Uncertainties in fragment energy calibrations were about 2%.

III. FRAGMENT SPECTRA

Since neutrons were recorded only in coincidence with fragments, a discussion of the fragment spectra will be useful. Figures 2 and 3 show linearized ΔE-E fragment identification plots for the Ho target for singles fragments at angles of 10° and 23°, respectively. One can see that we had excellent element separation and in many cases good isotope separation. In sorting the neutron data, gates were set across the fragment element groups of Li, Be, B, and C. Figures 4 and 5 show the singles fragment energy spectra. (The 30° fragment data for the Ho target were taken during an earlier experiment.[38])

By examining Figs. 2–5, one can obtain qualitative information about the reaction mechanism as a function of fragment angle. For example, in Fig. 2 (for fragments at 10° and Ho as the target) two features stand out clearly. First, all fragments are most prominent at energies near the beam energy per nucleon. Second, the N fragments stand out as distinct, with essentially no high energy fragments with $Z > 7$ being observed. Evidently, the processes leading to high energy fragments favor $Z \leq Z_{\text{beam}}$. This skewing of the charge distribution to $Z \leq Z_{\text{beam}}$ has also been observed for fragments near the grazing angle in the $^{12}C + {}^{158}Gd$ and $^{20}Ne + {}^{150}Nd$ systems at slightly lower beam energies (9–16 MeV/nucleon).[39] Processes such as projectile fragmentation and stripping would be possible candidates for the reaction mechanism. On the other hand, an examination of Fig. 3, where the fragment angle is 23°, shows that neither $Z = 7$ nor the beam energy per nucleon occupies a unique position, indicating that memory of the entrance channel has been lost. Suitable candidates for this process might be partial orbiting or fragment emission from a localized hot source.

The fragment energy spectra displayed in Figs. 4 and 5 for the Ho and Ni targets show the evolution of spectral shape as a function of angle. For fragments near the grazing angle, 8° for Ho and 4° for Ni, one sees the spectra dominated by a broad peak at energies corresponding to near-beam velocities. This dominating component corresponds to the quasielastic peak from projectile fragmentation in very peripheral collisions.[50] As the fragment angle increases, one sees the quasielastic component steadily decrease and essentially disappear for fragment angles of 23° and larger. The strongly damped component correspond-

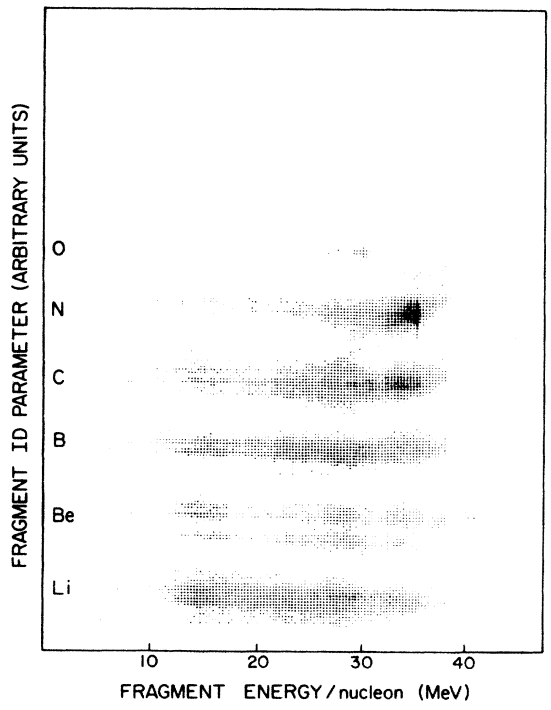

FIG. 2. Linearized ΔE-E fragment identification plot for fragments at 10° for the Ho target. Element groups are identified on the left.

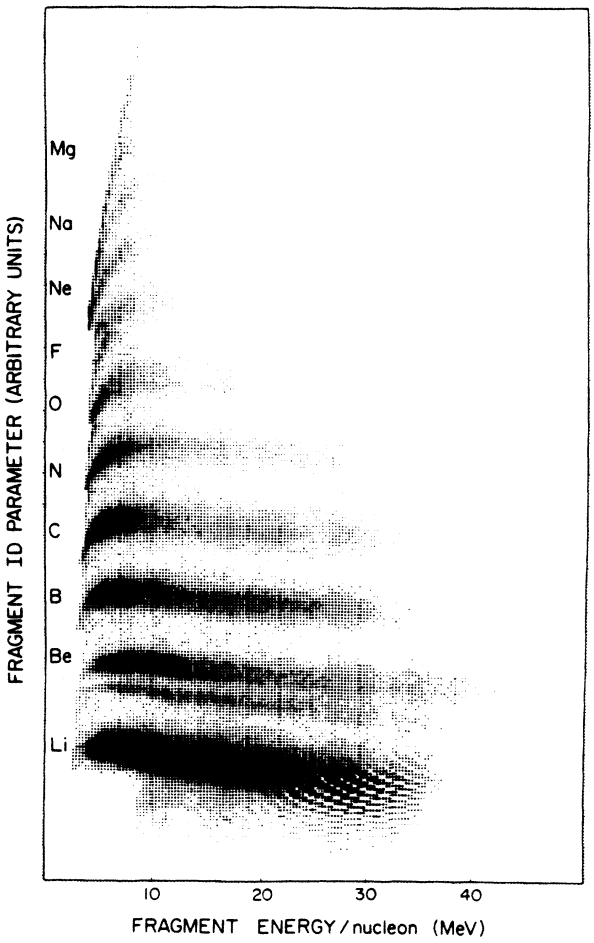

FIG. 3. Same as Fig. 2 except that fragments are at 23°.

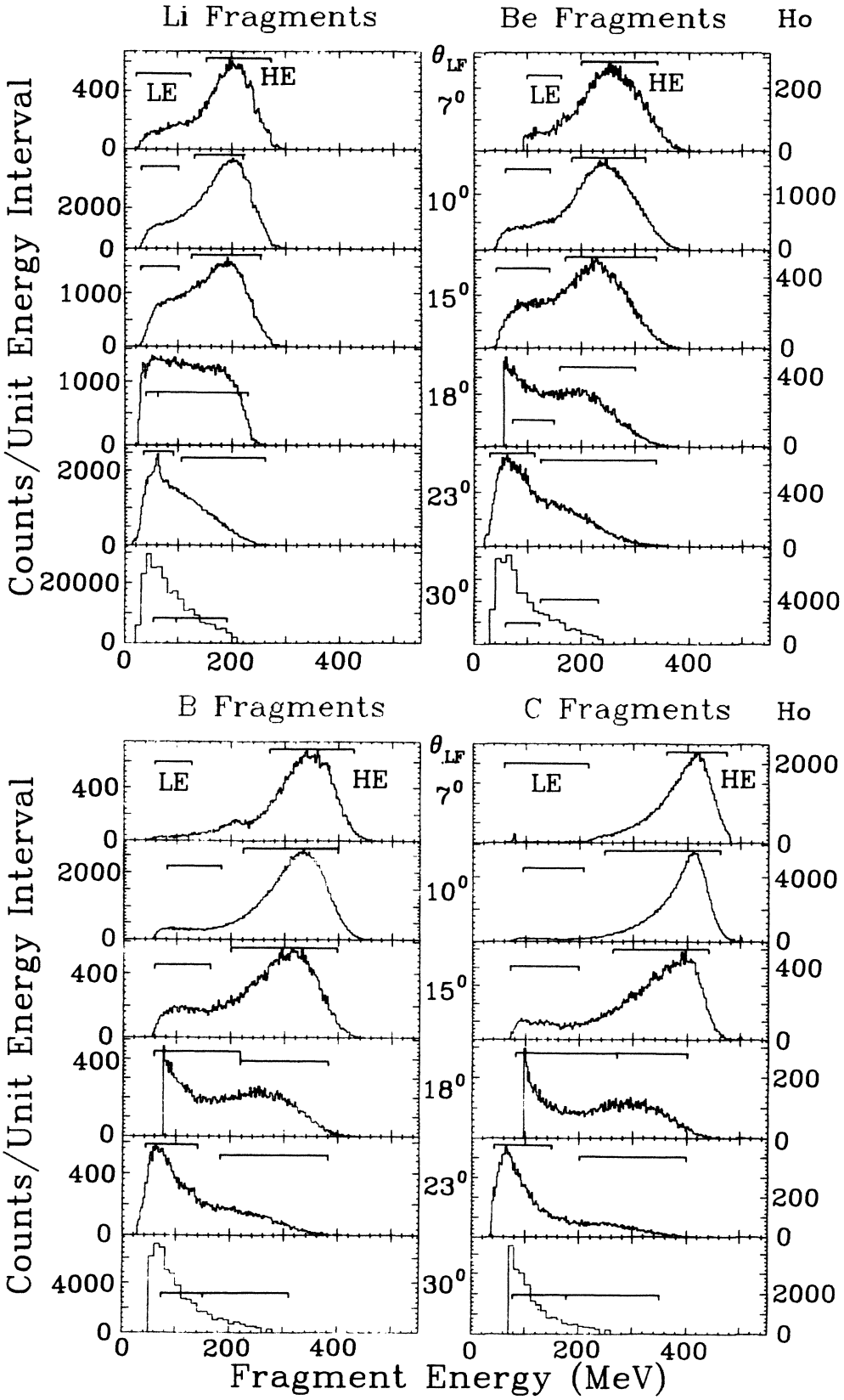

FIG. 4. Inclusive energy spectra for fragments of Li, Be, B, and C at angles of 7°, 10°, 15°, 18°, 23°, and 30° for the Ho target. Indicated on each spectrum are the high energy (HE) and low energy (LE) gates used in analyzing the coincident neutron spectra.

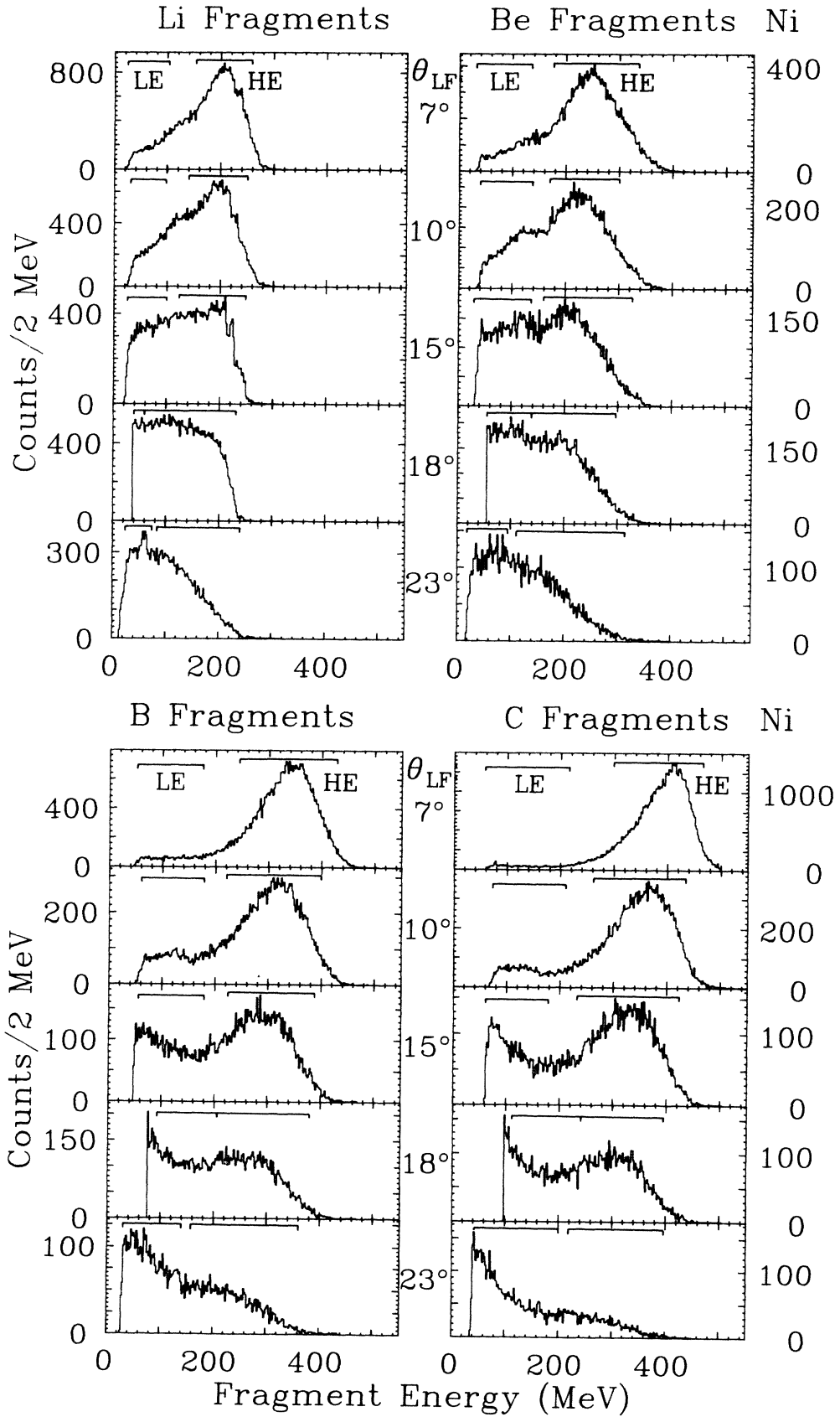

FIG. 5. Same as Fig. 4 except that the target is Ni and the angular distribution stops at 23°.

ing to low energy fragments from more central collisions exists at all the angles studied. For Ho at 30° this is the only component present, and the spectrum seems to be falling off nearly exponentially with energy. With these spectra indicating two kinds of collisions, namely central and peripheral, we selected corresponding low energy (LE) and high energy (HE) fragment gates for the neutrons and then separately analyzed the coincident neutron spectra for the two kinds of collisions.

There is a possibility that ^{8}Be could be misidentified as ^{7}Li in our fragment telescopes from the reaction $^8\text{Be} \rightarrow 2\alpha$ if both alpha particles enter the detector.[51] Based on the solid angles of the collimators and the average energy of the Be fragments within the LE and HE gates, we estimate that less than 1% of all ^{8}Be fragments result in both alpha particles entering the same detector. Unless ^{8}Be is produced with an anomalously high abundance in comparison to neighboring isotopes, this effect is negligible for the present work.

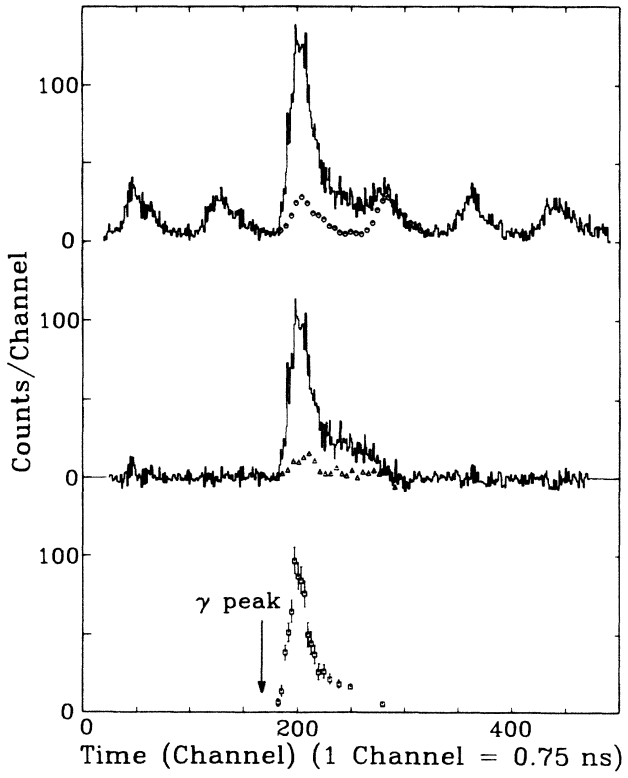

FIG. 6. Sample neutron time-of-flight (TOF) spectrum illustrating the level of accidental coincidences and of background events. Displayed at the top is the raw TOF data, with the contribution from accidental coincidences indicated by circles. The middle spectrum has been corrected for accidental coincidences, and the contamination from background (scattered) neutrons is indicated by the triangles. The bottom spectrum has been corrected for both background events and accidental coincidences and represents the "true" neutron TOF spectrum. Gamma-ray events have been suppressed using pulse-shape discrimination, but the position of the gamma-ray peak is indicated by the arrow.

IV. NEUTRON SPECTRA

The neutron energies were determined by time-of-flight (TOF). Figure 6 shows a neutron TOF spectrum along with the accidental coincidences (top) and background neutrons (middle). The final "true" TOF spectrum is shown at the bottom of the figure. The reference time in the neutron TOF spectra was determined by the position of the gamma-ray peak due to fragment–gamma-ray coincidences. The gamma-ray events have been suppressed in Fig. 6 using pulse shape discrimination, but the position of the gamma peak is indicated by an arrow. In the transformation from TOF spectra to energy spectra, the detector efficiency and an attenuation correction were folded in. The efficiency was calculated with a Monte Carlo code developed by Cecil *et al.*[52] and then compared with an efficiency from a code developed earlier by Kurz.[53] The two calculations agreed with one another, and both agree with data to better than 10%.[52,53] Although the efficiency is energy dependent, a typical value is 10%. The attenuation factor corrects for the attenuation of neutron flux by material lying between the target and the detector. This correction is also energy dependent, but again 10% is a typical value.

Figure 7 shows a neutron velocity scatter plot of invariant cross section for neutrons in coincidence with high energy boron fragments at 10°. The arrow in the figure indicates the average velocity vector of the fragment, and the cross section is proportional to the darkness of the lines. One notices that there are many high velocity neutrons at the forward angles, especially at $\theta_n = \pm 10°$, whereas at the

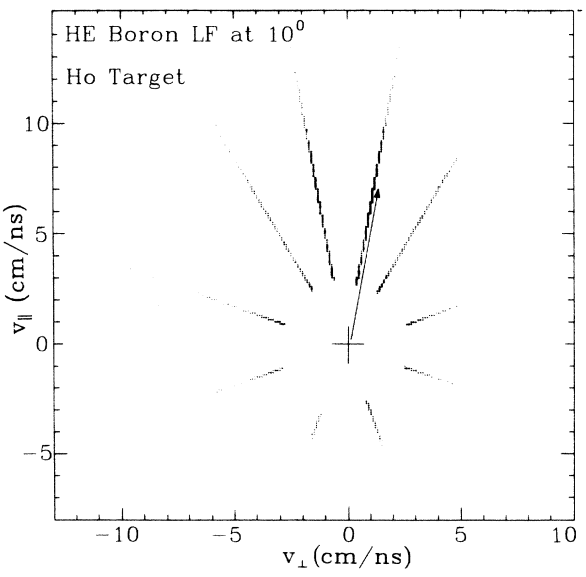

FIG. 7. Velocity scatter plot of invariant cross section for neutrons in coincidence with high energy boron fragments at 10° for the Ho target. Intensity of the lines is proportional to the yield. The abscissa corresponds to the component of the neutron velocity perpendicular to the beam direction and the ordinate to the parallel component. The arrow indicates the average velocity vector of the boron fragments.

back angles, there are very few high velocity neutrons. A very interesting feature can be seen at the middle angles of $\theta_n = \pm 70°$ and $\pm 110°$: There are more high velocity neutrons on the side of the beam opposite that of the fragment, verifying an earlier observation.[38]

Examples of neutron energy spectra are given in Figs. 8 and 9 for the Ni target and in Fig. 10 for the Ho target. The solid and dashed lines in Figs. 8 and 9 correspond to moving-source fits which will be discussed below. The ordinate in Figs. 8 and 9 is differential multiplicity in units of neutrons/(MeV sr) per detected fragment. Multiplicity was obtained by dividing neutron coincidence cross section by the fragment singles cross section for the appropriate fragment gate. The fragment singles cross sections used in this transformation are listed in Table I.

The coincident fragments in Fig. 8 are high energy carbons at 7°, and the inset gives the carbon spectrum. In this figure one can identify three distinct components of the neutron spectra. A low energy, nearly isotropic component dominates at $\theta_n = \pm 160°$; it corresponds to neutrons evaporated from a slowly moving targetlike source (TLS). At $\theta = \pm 10°$ one can see definite structure at energies between 15 and 45 MeV. This structure results from neutrons emitted from specific discrete states of excited projectilelike fragments of carbon nuclei.[43] The structure is centered around 30 MeV, which corresponds to the average velocity of the carbon fragments. The spread results from the addition of source and neutron velocities. With the gate used for the coincident high energy carbon fragments, a decay energy of only 2 MeV is sufficient to produce laboratory neutron energies between 15 and 45 MeV. Emission from discrete states of the projectilelike fragment has been seen by others for neutrons[29,30,33,40,41] and for α particles.[54] In addition to the TLS and the light-fragment components, one can see at middle angles in Fig. 8 a distinct third component of high energy neutrons. This component appears thermal in shape, has a much flatter slope than the TLS component, and exhibits an interesting asymmetry at $\pm 70°$ and probably at $\pm 110°$. There are more high energy neutrons seen at 70° on the side opposite the detected fragment than on the same side. This asymmetry was seen in an earlier study of the

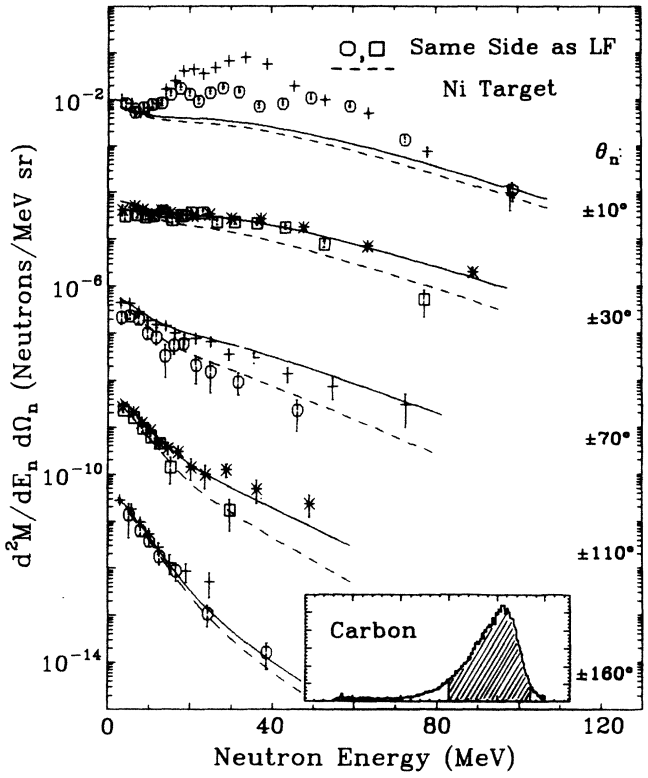

FIG. 8. Differential multiplicity spectra (neutrons/MeV sr per detected fragment) for neutrons in coincidence with high energy carbon fragments at 7° for the Ni target. The spectra are plotted in symmetric angle pairs, each offset from the next by a factor of 100, with the spectra at the top having the scale as indicated. The curves correspond to moving-source fits with a TLS and an IRS (see the text). The open symbols and dashed lines correspond to neutrons on the same side of the beam as the detected fragment, while the closed symbols and solid lines correspond to neutrons on the opposite side. The gate set across the fragment energy is shown as the hatched region in the inset. The multiplicity, temperature, energy per nucleon, and angle of the TLS (IRS) are 0.35 (0.34), 3.40 MeV (10.00 MeV), 0.12 MeV/nucleon (11.00 MeV/nucleon) and $-18.5°$ ($-10.5°$).

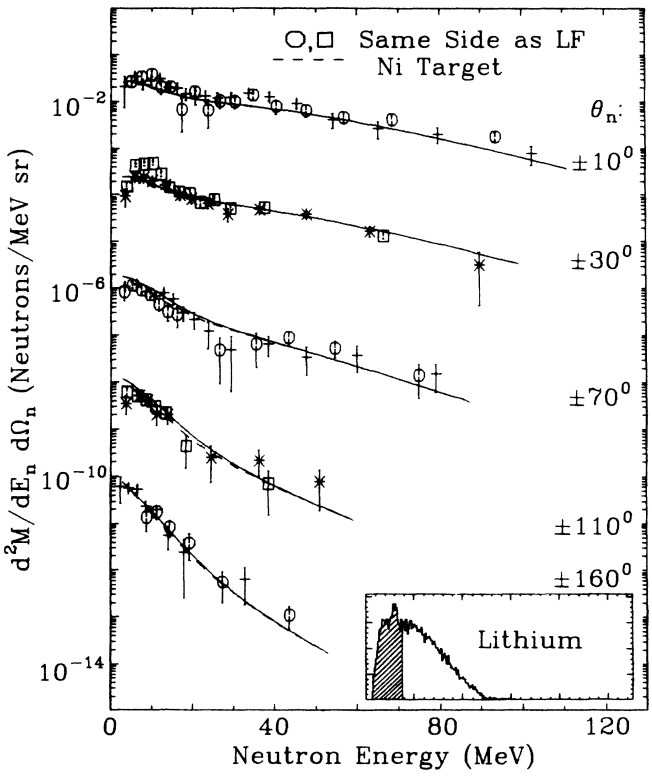

FIG. 9. Same as Fig. 8 except that the neutrons are in coincidence with low energy lithium fragments at 23°. The multiplicity, temperature, energy per nucleon, and angle of the TLS (IRS) are 1.63 (1.07), 4.23 MeV (12.27 MeV), 0.58 MeV/nucleon (12.11 MeV/nucleon), and $-7.6°$ (0.0°).

$^{14}N + {}^{165}Ho$ system for very peripheral collisions,[38] and we have now observed it in the $^{14}N + Ni$ system, also for peripheral collisions.

Figure 9 shows the neutron spectra in coincidence with low energy Li fragments at 23°. Again three components can be identified. The low energy, nearly isotropic TLS component is most easily distinguished at $\theta_n = \pm 160°$. The contribution from discrete neutron emitting states of the light fragment causes a small "peak" at about 8 MeV in the neutron detector at $+30°$ (this is the neutron detector nearest to the fragment direction of $+23°$). The "peak" is roughly centered around the average energy per nucleon of the detected fragment. The third component, corresponding to high energy neutrons at middle angles, is prominent in this spectrum, too, with one notable exception: There is no visible asymmetry at $\theta_n = \pm 70°$. This lack of asymmetry is also consistent with the observations of Ref. 38 on the $^{14}N + {}^{165}Ho$ system, where no neutron asymmetry was observed for strongly-damped reactions.

Summarizing the systematics of the asymmetry, we have observed for the Ho target that the asymmetry exists only for high energy fragments at 7° and 10°, whereas the grazing angle is about 8°. For the Ni target the asymmetry was seen only for high energy fragments at 7°, whereas the grazing angle is about 4°. For both targets the asymmetry is strongest for fragments of mass just below, or equal to, the projectile mass. Since the asymmetry is strongest for high energy, near-projectile-mass fragments close to the grazing angle, it seems to be associated with the most peripheral interactions.

Instrumental asymmetry has been checked by examining the neutron spectra at symmetric angle pairs for a coincident fragment at 15° out-of-plane directly below the beam. Examples of such spectra are displayed in Fig. 10. As all of the coincident Li, Be, B, and C fragments were used, the statistical accuracy of the comparisons is high. There is no observable asymmetry in these spectra.

A more subtle possible cause of an asymmetry arises from the recoil of the light fragment after it emits a particle. It has been shown[27,31,32,39,54] that under certain conditions, asymmetries in the same sense as we observe can be caused by the recoil of the emitter. Considering the asymmetries in Fig. 8 as an example, we first note that the angular distribution of the parent fragments is very steeply falling (see Fig. 5). So there are many more fragments inside of 7° (the angle of the fragment detector) than outside of 7°. Therefore, more fragments recoil into the telescope from inside of 7° by emitting a neutron to the side opposite than recoil into the telescope from outside of 7° by emitting a neutron to the same side. This effect has

TABLE I. Fragment singles cross sections.

	Ho target		Ni target	
	$d\sigma/d\Omega$ (mb/sr)	$d\sigma/d\Omega$ (mb/sr)	$d\sigma/d\Omega$ (mb/sr)	$d\sigma/d\Omega$ (mb/sr)
Fragment	LE	HE	LE	HE
$\theta = 7°$				
Li	220	973	146	720
Be	76	586	92	437
B	62	1405	80	880
C	96	3045	81	1330
$\theta = 10°$				
Li	120	426	122	401
Be	42	241	83	198
B	40	436	63	285
C	28	630	58	336
$\theta = 15°$				
Li	92	192	99	175
Be	42	65	55	72
B	33	73	46	76
C	23	47	36	75
$\theta = 18°$				
Li	35	196	37	222
Be	36	39	44	60
B	35	28	59	47
C	20.5	12.7	31	37
$\theta = 23°$				
Li	75	65	53	93
Be	28	22	32	39
B	27	12.0	34	28
C	17.7	5.1	38	12.5

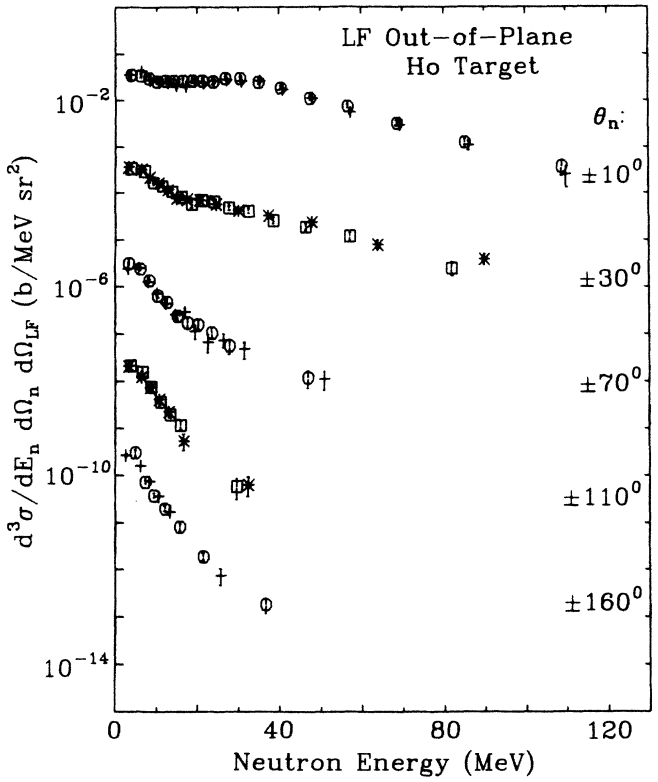

FIG. 10. Neutron spectra in coincidence with all fragments of $Z \geq 3$ moving at 15° out-of-plane. The spectra are plotted in symmetric angle pairs, each offset from the next by a factor of 100, with the spectra at the top having the scale as indicated.

been studied with a computer simulation.[55] It has been found that even though an asymmetry of the sense observed can be created, the calculated energy and angular distribution do not agree with the data. In essence, a fragment moving at near-beam velocity towards the 7° telescope cannot contribute significantly to the high energy neutrons at middle angles, where the asymmetry is observed.

For a comprehensive treatment, we fit the data in terms of two thermal, moving sources. We have seen that the neutrons seem to originate from three sources: an excited light fragment, an excited TLS, and a preequilibrium source. Based upon the structure seen in all neutron spectra associated with the light fragment, we feel that there is sufficient neutron yield from nonthermal, discrete-state origins to warrant not using the standard thermal source analysis on these spectra. Contribution from the light-fragment source is relegated to a separate analysis where careful consideration of discrete-state emission is given.[43] In this paper we study the behavior of only the TLS and the preequilibrium (IRS) neutrons.

A thermal parametrization is predicated upon the idea of evaporation of nucleons from a "hot" nucleus. The spectrum takes the following form in the rest frame of the emitter:[56]

$$N(E_n) \propto E_n^{\alpha} e^{-E_n/\tau}, \tag{1}$$

where E_n is the energy of the neutron and τ is a temperature parameter. $\alpha = 1$ corresponds to single neutron "surface emission," whereas $\alpha = \frac{1}{2}$ corresponds to volume sampling ("volume emission"), from a hot Fermi gas. In both cases, the temperature parameter τ is the temperature T of the daughter nucleus after single neutron emission. The value $\alpha = \frac{5}{11}$ corresponds to multiple neutron emission, and then τ is an effective temperature parameter related to the temperature T of the daughter nucleus after the first neutron emission by $T = (\frac{12}{11})\tau$.[56]

The IRS is typically in a very excited state at an excitation-energy per nucleon near to or exceeding the binding energy, so volume emission (with $\alpha = \frac{1}{2}$) should be the most suitable choice for this source. The TLS most probably emits more than one neutron, indicating that $\alpha = \frac{5}{11} \approx \frac{1}{2}$. So we use the same prefactor $\sqrt{E_n}$, i.e., $\alpha = \frac{1}{2}$, for both sources. Each source introduced is assumed to emit neutrons isotropically in its rest frame. The spectra of these neutrons are then transformed into the lab frame, taking the motion of the emitting source into account. The sum of these two contributions, then, written as a differential multiplicity takes the following form:

$$\frac{d^2M}{dE_n d\Omega_n}(E_n,\theta_n) = \sum_{i=1}^{2} \frac{M_i \sqrt{E_n}}{2(\pi\tau)^{3/2}} \exp\left\{ -\left[\frac{E_n - 2\sqrt{(\epsilon_i E_n)}\cos(\theta_i - \theta_n) + \epsilon_i}{\tau_i} \right] \right\}, \tag{2}$$

where the index i sums over the two sources. Equation (2) predicts the number of neutrons/(MeV sr) per detected light fragment. E_n and θ_n are the neutron energy and angle, respectively, while M_i, τ_i, ϵ_i, and θ_i are the neutron multiplicity, nuclear temperature parameter, kinetic energy per nucleon, and angle of the ith source, the velocity of which is assumed to lie in the reaction plane defined by the beam velocity and the velocity of the detected fragment. Equation (2) is then fitted to the data by minimizing the χ^2, thus allowing extraction of multiplicities, temperatures, and velocities for the TLS and IRS components of the reaction.

Neglecting the three angles nearest to the direction of the coincident light fragment, we fitted the data at seven angles. (With the inclusion of a projectilelike source emitting neutrons from the decay of discrete states, all ten spectra can be fitted.[44]) The solid and dashed lines in Figs. 8 and 9 are examples of the results of such two thermal moving source fits, and the parameters of these fits are listed in the figure captions. All fits contain eight

parameters, and typical values of the χ^2 per degree-of-freedom are between 1 and 2.

V. THE FIT PARAMETERS

The moving source parametrization allows one to describe a large body of data with a few parameters. In this section we examine the resulting fit parameters for both the TLS and the IRS as functions of the coincident fragment: its species, its energy, and its angle. In such an examination we search for any trends or behaviors in the fit parameters that might serve as clues to the reaction mechanism. First the TLS fit parameters will be discussed, along with the results from a two-body kinematics calculation and also from the statistical code CASCADE.[2] Then the IRS fit parameters will be examined.

Figures 11–13, 15, 17–19, and 21 are plots of the various fit parameters of the TLS and the IRS as functions of the angle of the coincident light fragment. In each of these figures the top four plots correspond to the coincident fragments of Li, Be, B, and C for the Ho target; the bottom four plots correspond to the same fragments, but the target is Ni. The error matrix produced in the fitting procedure gave errors that were generally unrealistically small because they did not account for the "structure" (secondary minima) in the χ^2 space. Hence, they were not incorporated into error bars for the fit parameters. Also included in these plots are fit parameters extracted from data obtained in an earlier experiment[44] on the $^{14}N + {}^{165}Ho$ system at 35 MeV/nucleon for fragment angles of 10° and 30°. These parameters were therefore extracted from an independent set of data in an independent analysis. Their deviations from the values of the present experiment are a measure of systematic errors.

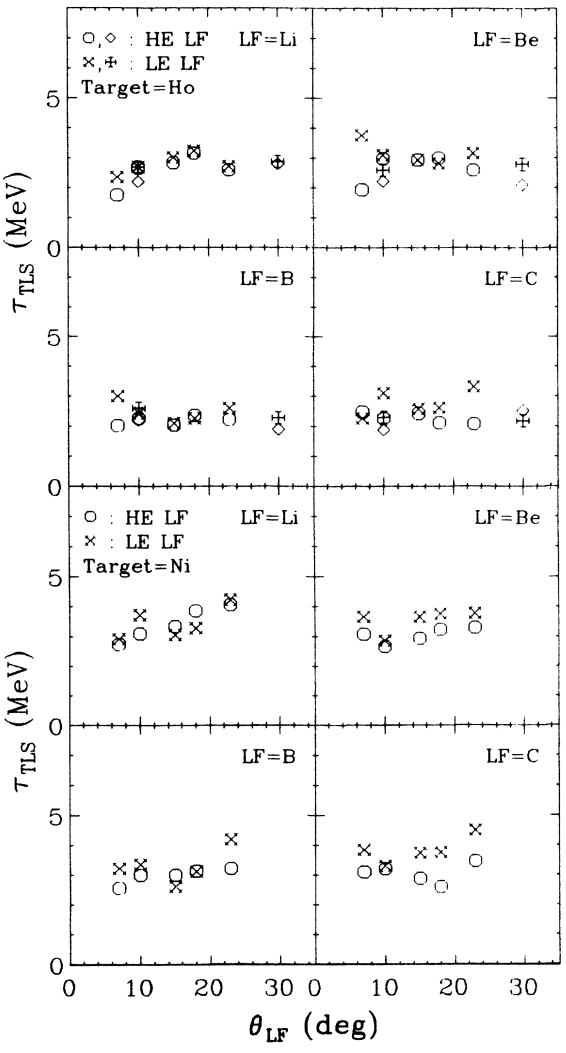

FIG. 11. The TLS temperature parameter, τ_{TLS}, versus fragment angle for the Ho target (top) and Ni target (bottom). Each quadrant represents a different fragment. The diamond and vertical-cross plotting symbols at 10° and 30° correspond to an independent set of data and analysis (see the text). Open symbols correspond to high energy light fragments (HE LF) and closed symbols to low energy light fragments (LE LF).

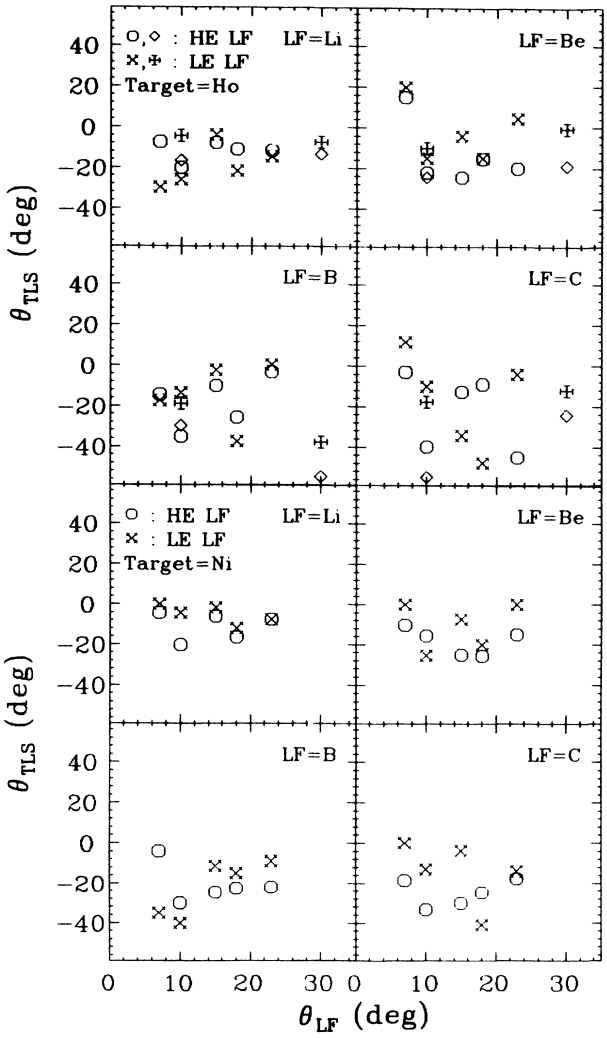

FIG. 12. The TLS angle, θ_{TLS}, vs fragment angle. The dotted line corresponds to an angle of 0°. The format is the same as that of Fig. 11.

A. TLS parameters

Figure 11 is a display of the TLS temperature parameter τ_{TLS} as a function of fragment angle. There seems to be no clear dependence of τ_{TLS} on either the angle or the energy of the fragment. The temperature of the TLS varies between 2 and 3 MeV for the Ho target, whereas for the Ni target the temperature is higher, at 3 to 4 MeV.

Figure 12 is a plot of the angle of the TLS vs the angle of the detected light fragment. Since the TLS is moving very slowly, the direction of its motion cannot be determined very precisely by fits of the neutron spectra; hence the angle parameter displays considerable scatter. One notable feature of these plots is that, with few exceptions, θ_{TLS} is negative, that is, opposite to the side of the detected light fragment. The TLS clearly participates in the momentum sharing.

Figure 13 shows the kinetic energy per nucleon of the target source, E/A_{TLS} plotted as a function of fragment angle. E/A_{TLS} displays no systematic dependence on the energy of the detected fragment but tends to increase with θ_{LF}. For a given fragment angle, E/A_{TLS} for the Ni target is typically a factor of 5–10 larger than for the Ho target.

To establish a reference for E/A_{TLS} we performed two-body kinematics calculations. The reaction was assumed to be $^{14}N + \text{target} \rightarrow LF + TLS$. From the measured values of mass and energy of the LF at each LF angle, we determined its momentum, and by momentum conservation, the momentum of the TLS. With the two-body assumption, the mass of the LF gave us the mass of the TLS and, hence, its E/A. The solid and dashed lines

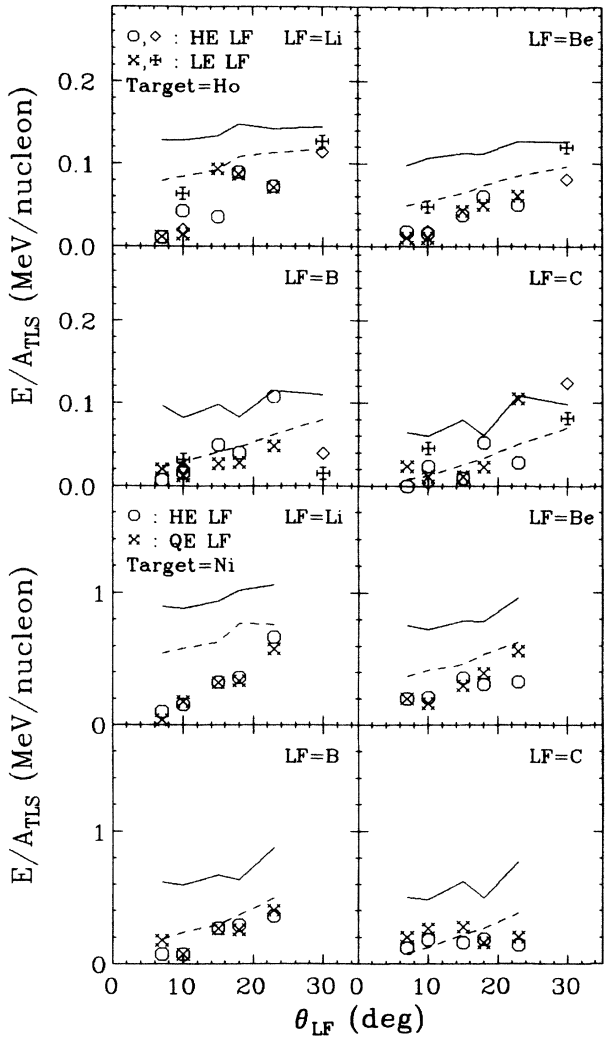

FIG. 13. The TLS kinetic energy per nucleon, E/A_{TLS}, vs fragment angle. The solid and dashed lines correspond to a two-body calculation for reactions leading to low energy and high energy fragments, respectively. The format is the same as that for Fig. 11. (Note the difference in scale between the Ho and Ni data.)

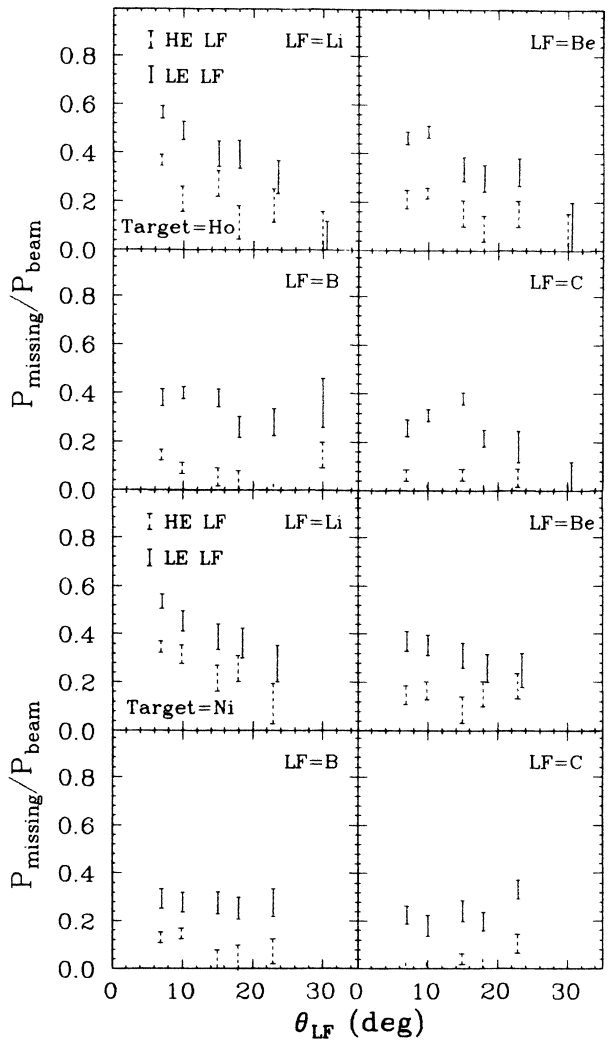

FIG. 14. The fraction of the beam momentum "missing" versus fragment angle. The fraction was determined by the difference between a two-body calculation and the data. The format is the same as that of Fig. 11.

in Fig. 13 are the results of these calculations. The "structure" in the lines is due to the various gates set across the energy of the LF (see Figs. 4 and 5). With few exceptions, the calculation predicts a larger E/A_{TLS} than is observed, the discrepancy being largest for low energy fragments. This discrepancy is a clear indication that the reaction is not binary, at least not in the simple sense assumed in the calculation. There is some component of the reaction carrying away momentum that is "missed" by our detectors.

Figure 14 is a plot of the fraction "missing momentum"/beam momentum as a function of LF angle for the Ho target (top) and the Ni target (bottom). The missing momentum is assumed to be parallel to the beam axis and corresponds to the difference between the calculated and the observed values in Fig. 13. The large error bars in Fig. 14 are due to the inherent uncertainties in θ_{TLS} and E/A_{TLS}. The value of the fractional missing momentum varies between 0.5 and 0.0 for both targets and is largest when we detect a low energy fragment. In addition, for both targets the missing momentum is largest for Li fragments at small angles and smallest for C fragments. It appears that as the amount of LF energy damping increases, and also as $A_{\mathrm{projectile}} - A_{\mathrm{LF}}$ increases, so too does the amount of missing momentum. This is qualitatively similar to what has been observed in projectilelike-fragment—fission-fragment coincidence studies.[24,57] In those investigations the missing momentum was seen to increase with projectilelike fragment damping, and was attributed to emission of a "jet" of particles preferentially into the forward direction.[57] We will discuss possible origins of the missing momentum later.

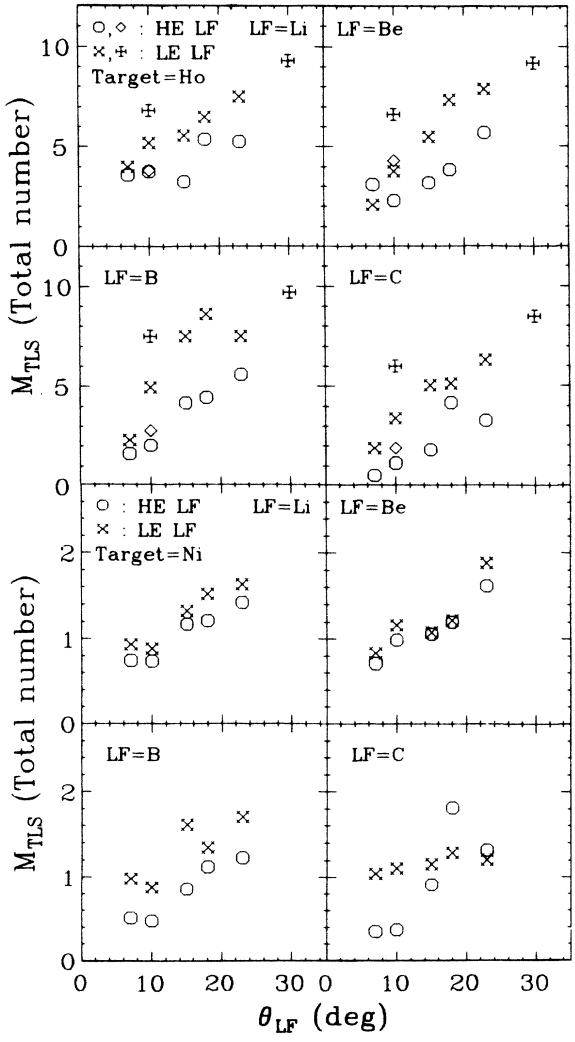

FIG. 15. The measured TLS multiplicity, M_{TLS}, vs fragment angle. The format is the same as that for Fig. 11. (Note the difference in scale between the Ho and Ni data.)

Figure 15 shows the measured TLS multiplicity as a function of LF angle, where measured TLS multiplicity refers to the total number of neutrons emitted by the TLS per detected LF. One immediately notices that the TLS multiplicities for the Ho target are much higher than those for the Ni target. But multiplicity varies directly with excitation energy. As discussed below, excitation energy can be calculated from the fitted temperature parameter, and estimates of E^*_{TLS} averaged over θ_{LF} give 150 MeV and 100 MeV for the Ho and Ni TLS, respectively. So based upon excitation energy alone, one would expect the Ho TLS multiplicity to be larger than the Ni TLS multiplicity. In addition, due to the lower Z of Ni, the Ni TLS has a smaller Coulomb barrier than the Ho TLS, and proton or alpha emission can compete with neutron emission.

There is a distinct increase in measured TLS multiplicity with θ_{LF}, and the multiplicities for the low energy fragment gates are considerably larger than for the corresponding high energy gates. To understand these trends, we note that it is quite possible for the reaction to produce a LF, especially a high energy LF, without exciting the target fragment to above the neutron-emission threshold, hence forming a TLS; there is competition between transfer reactions and projectile breakup. The observation that the temperature of the TLS is approximately independent of θ_{LF} (Fig. 11) suggests that the multiplicity

TABLE II. Calculated TLS multiplicities for central collisions using CASCADE, JULIAN,[a] and PACE.[b]

Nucleus	J ($\hbar$)	E^* (MeV)	Multiplicity
^{58}Ni	40	83	1.2
^{58}Ni	5	125	1.6
^{58}Ni	40	125	1.7[c]
^{60}Ni	40	83	2.2
^{60}Ni	40	150	3.8[c]
^{165}Ho	80	100	7.7
^{165}Ho	80	195	12.0[c]
$A=163-170$		100 MeV	5.5[a]
$A=163-170$		200 MeV	10.5[a]
$A=64$		60–80 MeV	3.0[b]

[a]Taken from Ref. 17.
[b]Taken from Ref. 40.
[c]Indicates the final values used.

should also be approximately independent of θ_{LF}. We interpret a low measured TLS multiplicity at small θ_{LF}, then, as an indication that not every reaction resulting in a detected LF necessarily produces a TLS.

For comparison we used the statistical code CASCADE (Ref. 2) to calculate the total neutron emission from a TLS. The most important input to CASCADE is the excitation energy. Using the fitted temperature parameter (corresponding to the TLS component of the neutron spectra) and the neutron separation energy S_n allows one to estimate the average TLS excitation energy E^* before neutron emission. This is done with the thermodynamical relation

$$E^* = aT^2 + S_n \ , \tag{3}$$

where $a = A/8$ is the density-of-states parameter, $S_n \approx 8$ MeV, and $T = (\frac{12}{11})\tau$ corresponds to the temperature of the daughter fragment after single neutron emission. $\tau_{TLS} = 4$ MeV is a typical TLS temperature parameter for the Ni target for a fragment angle of 23°, where the experimentally determined multiplicity is largest. Averaging over target isotope then gives a calculated multiplicity of about 2.3 neutrons per excited Ni TLS. Figure 15 shows that the measured TLS multiplicity for low energy fragments at $\theta_{LF} = 23°$ is about 1.6, i.e., 70% of the calculated value. CASCADE was also used for the $^{14}N + {}^{165}Ho$ system for an excitation energy of 195 MeV, and the resultant total neutron multiplicity was 12. The average measured TLS multiplicity for a low energy gate on fragments at 30° (corresponding to the maximum measured result for the Ho TLS) is about 9.2, i.e., 77% of the calculated result. The results of the CASCADE calculations for both the Ni and the Ho target are contained in Table II. Though comparisons of CASCADE calculations with data for systems at high excitation energy are not readily available, we believe our predicted values to about 20%.

At this point we review some multiplicity results obtained by other investigators on similar systems. Tserruya *et al.* have studied the $^{86}Kr + {}^{166}Er$ system at 11.9 MeV/nucleon (Ref. 17) and extracted multiplicity as a function of excitation energy both for the targetlike and projectilelike sources. They then compared their values to the results of a calculation using the Monte Carlo code JULIAN. For a TLS of $A = 163-170$ with $E^* = 200$ MeV, their observed TLS multiplicity was 8. Their calculated multiplicity using $a = A/8$ was 10.5 for 200 MeV excitation and 5.5 for 100 MeV excitation. These values are included in Table II for comparison. Their calculated multiplicity was also larger than their measured multiplicity.

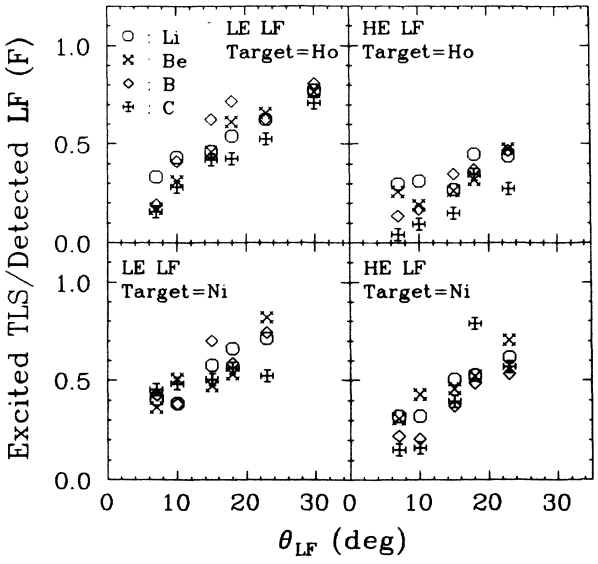

FIG. 16. The fraction of excited targetlike sources (TLS) formed per detected light fragment (LF) as a function of light fragment angle. The top two plots are for the Ho target and the bottom two for the Ni target. For each target, the data on the left are for reactions leading to low energy light fragments (LE LF) and the data on the right for high energy light fragments (HE LF). Each quadrant has F plotted for each of the four light fragments (Li, Be, B, C).

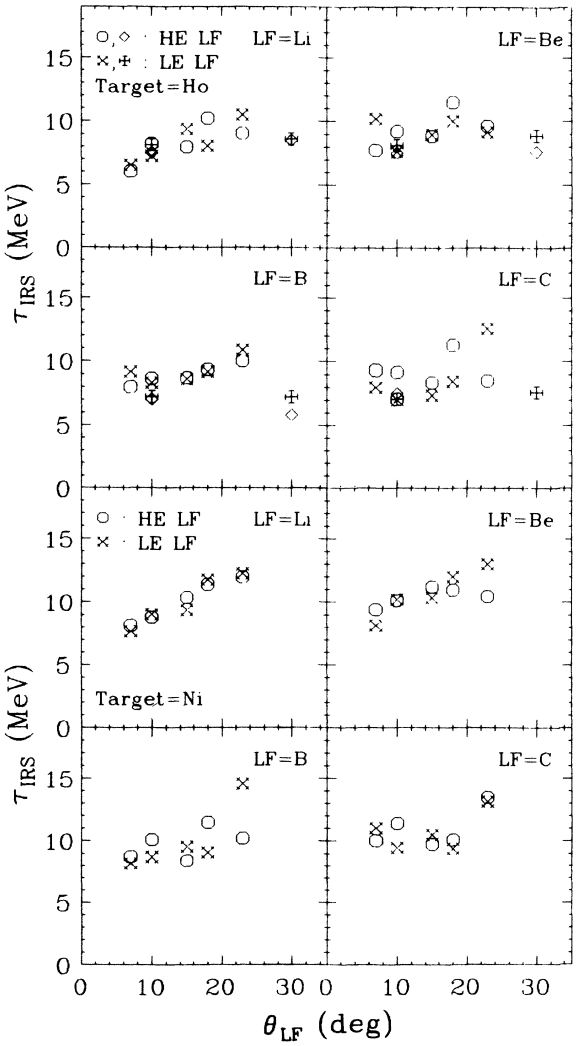

FIG. 17. The IRS temperature parameter, τ_{IRS}, vs fragment angle. The format is the same as that of Fig. 11.

To bring the calculation into agreement with their data, Tserruya *et al.* chose to adjust their density-of-states parameter to $a=A/20$. The possibility remains, though, that the discrepancy was due to the difference between the measured multiplicity per event and the multiplicity per created TLS as discussed above, and not to the choice of the density-of-states parameter. Lücking *et al.*[40] have studied the $^{16}O+{}^{64}Ni$ system at 7.5–12 MeV/nucleon, extracting experimental TLS and projectilelike fragment multiplicities and comparing with the evaporation code PACE. For a coincident O projectilelike fragment resulting in $E^*_{TLS}=60-80$ MeV, their experimental and calculated TLS multiplicities were 3.2 ± 0.8 and 3.0, respectively, indicating good agreement between measured and calculated multiplicity.

We have observed a dependence of the measured TLS multiplicity on LF angle and have interpreted this as evidence for angle-dependent competition between reactions leading to a TLS (such as transfer or incomplete fusion) and reactions not appreciably exciting the target nucleus (such as knockout or projectile breakup). Competition between transfer and projectile breakup has been clearly demonstrated by Jahnke *et al.*[58] for the $^{20}Ne+{}^{197}Au$ system at 15 MeV/nucleon by measuring total neutron multiplicities using a 4π neutron-multiplicity counter. But we believe that our observation is the first time a strong angle dependence has been demonstrated for this competition.

Taking the ratio of the measured TLS multiplicity to the calculated multiplicity gives one the fractional occurrence of an (excited) TLS per detected LF. This fraction, call it F, is plotted as a function of fragment angle and energy gate in Fig. 16. One notices the following: (1) F increases steadily with θ_{LF}, but at $\theta_{LF}=23°$ or 30° is still less than one. (We note that adjustment of the density-of-states parameter could bring F closer to 1 at 23° or 30°, as was pointed out in Ref. 17.) (2) F is larger for the low energy fragment gates than for the corresponding high energy gates. (3) At a given fragment angle F is slightly larger for the Ni target than for the Ho target. (4) The smallest values of F for both targets occur for high energy C fragments. Observations (1) and (2) are consistent with the idea that larger fragment angle and greater energy damping indicate longer interaction time between the projectile and target nuclei.[29] Longer interaction time creates a more favorable setting for transfer and partial fusion to occur, both of which lead to an excited TLS. Observation (3) is consistent with the fact that the grazing angle for the Ni target (4°) is smaller than for the Ho target (8°). So for fragments scattered through the same angle, the impact parameter is smaller and the projectile-target interaction greater for Ni than for Ho. Observation (4) may be attributed to the fact that some of the high energy fragments result from quasielastic scattering. When the fragment is carbon rather than lithium, beryllium, or boron, the smallest number of nucleons are lost from the fragment, thus maximizing the chance of scattering without forming a TLS.

B. IRS parameters

Figure 17 shows the temperature of the IRS as a function of fragment angle. There appears to be no single clear trend of τ_{IRS} with fragment angle common to both targets. In addition, there appears to be no significant difference in IRS temperature whether the gate is on fragments of low energy or high energy. The independence of τ_{IRS} on energy and angle of the fragment suggests that the IRS neutrons were produced at a very early stage of the reaction before the "final fate" of the projectile had been determined. Similar results were reported by Gemmeke *et al.*[37] in neutron-projectilelike fragment coincidence studies of the $^{16}O+Ni$ system at 6 MeV/nucleon as well as by Back *et al.*[24] and by Awes *et al.*[25] in light-particle–fission-fragment coincidence studies of $^{16}O+{}^{238}U$ at 20 MeV/nucleon. For the Ni target, the tempertures of the IRS are systematically higher than for the corresponding cases for the Ho target. A typical value of τ_{IRS} for the Ho target is 8.5 MeV whereas for the Ni target the average τ_{IRS} is closer to 10 MeV.

To try to understand what these fitted temperatures mean, we can derive a reference temperature with which

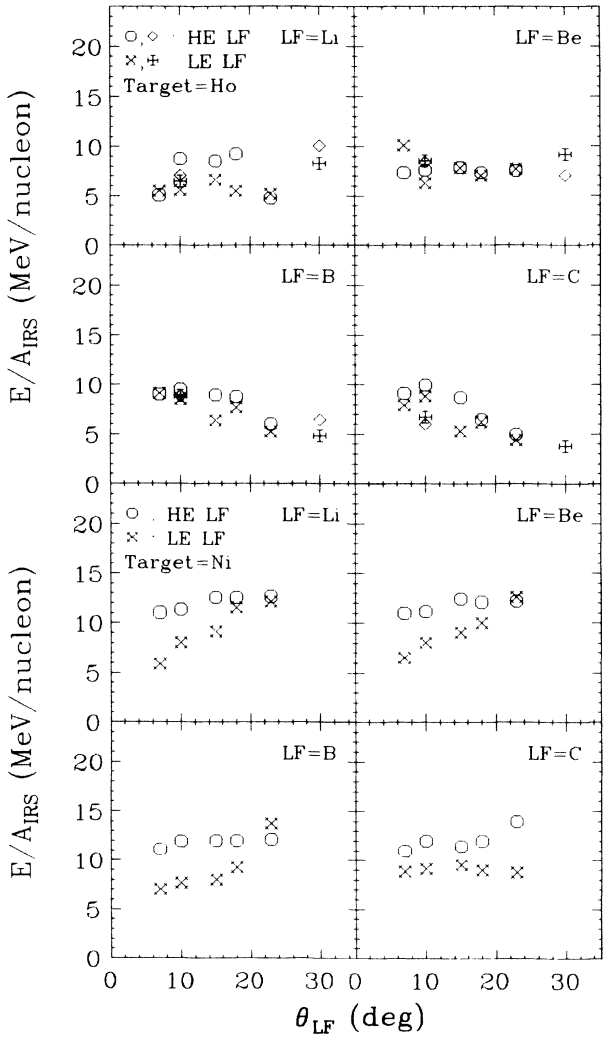

FIG. 18. The IRS kinetic energy per nucleon, E/A_{IRS}, vs fragment angle. The format is the same as that of Fig. 11.

to "calibrate" τ_{IRS}. Adopting the approach of Awes *et al.*,[25] we equate the region of overlap between the projectile and target with an ideal Fermi gas consisting of equal contributions from the target and projectile nuclei. The assumption of thermal equilibrium then corresponds to thermalization in the nucleon-nucleon center of mass frame, and allows one to predict a temperature [see Eq. (14) in Ref. 25]. With this method the predicted IRS temperature for both the Ho and Ni targets is about 11 MeV, slightly higher than that derived from the data. If one instead assumes that the overlap region consists of two target nucleons for every projectile nucleon, then the predicted IRS temperature is about 7 MeV, slightly lower than observed. So it appears that averaged over the lifetime of the hot source, each participating projectile nucleon interacts with between one and two target nucleons.

Figure 18 shows the kinetic energy per nucleon of the IRS vs fragment angle. There appears to be no single clear trend for the Ho target, though on the average the velocity of the IRS for high energy fragments is slightly higher than for the corresponding case of low energy fragments. Values of E/A_{IRS} for the Ho target range from about 5 to 10 MeV/nucleon, with an average of 7.5. For the Ni target, the values range from 6 to 13 MeV/nucleon, with an average of 10.5. For orientation we compare to the value of E/A corresponding to the nucleon-nucleon center of mass velocity in the lab frame at the point of projectile–target-nucleus "contact." For the Ho target the value is 7.7 MeV/nucleon and for Ni it is 8.2 MeV/nucleon. (The small difference between the two values is due to the difference in Coulomb barriers of the two systems.) Since the calculated values are within the ranges of the observed values, it may be that neutron emission occurs after a very rapid local thermalization, perhaps after a single nucleon-nucleon collision.[25]

Figure 19 shows the angle of the IRS as a function of the angle of the fragment. For the Ho target the only IRS angles that are significantly different from 0° occur for high energy fragments of B and C at $\theta_{LF}=7°$ and 10°. For the Ni target, the only significant nonzero θ_{IRS} occurs for high energy C fragments at 7°. In the nonzero cases the angle of the IRS is always negative, indicating that it is moving towards the side of the beam opposite to the direction of motion of the fragment. This is how the moving IRS reproduces the asymmetry of high energy neutrons at middle angles. In each case of nonzero IRS angle, the fragment is detected close to the grazing angle, indicating that the asymmetry is associated only with the most peripheral collisions.

It is interesting to note that such asymmetries in preequilibrium emission were not noticed until light-particle–projectilelike fragment coincidence measurements were made. Asymmetric preequilibrium emission

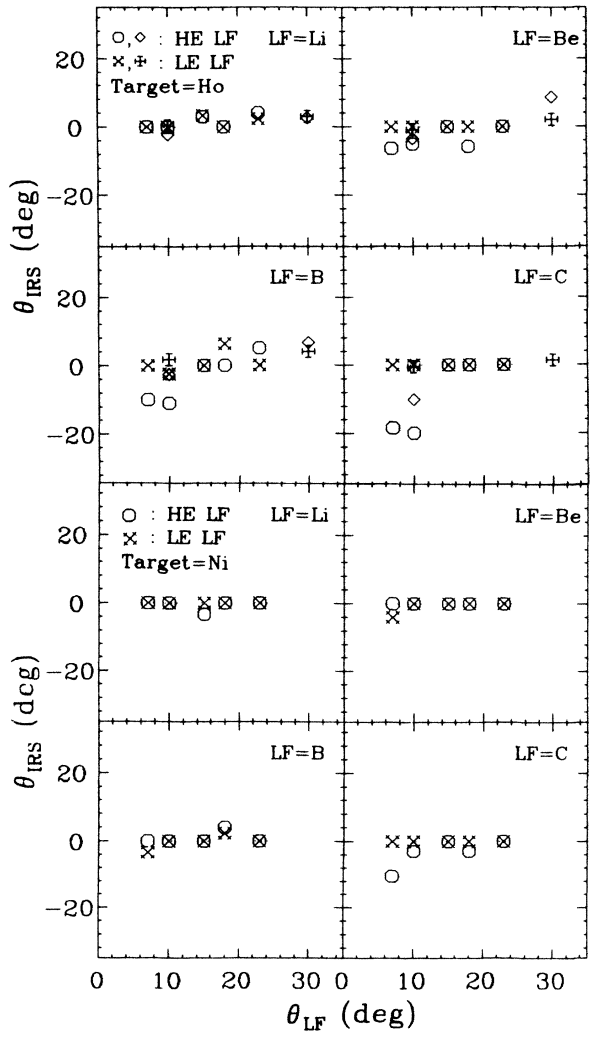

FIG. 19. The IRS angle, θ_{IRS}, vs fragment angle. The format is the same as that of Fig. 11.

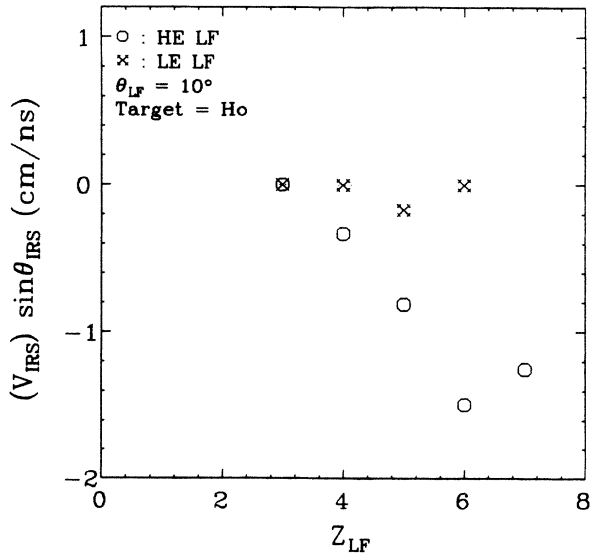

FIG. 20. The IRS transverse velocity, $(V_{IRS})\sin\theta_{IRS}$, vs fragment charge, Z_{LF}, for fragments at 10° for the Ho target. Open circles correspond to high energy light fragments (HE LF) and crosses to low energy light fragments (LE LF).

has now been seen in measurements of α particles in coincidences with projectilelike fragments in $^{16}O + Pb$ and $^{16}O + Au$ reactions at 9 and 20 MeV/nucleon (Ref. 16) and in neutron-projectilelike fragment coincidence measurements in $Kr + ^{166}Er$ reactions at 12 MeV/nucleon.[17] Both investigators saw an enhancement of preequilibrium particles on the same side as the detected fragment for quasielastic collisions and an enhancement on the opposite side for strongly damped collisions. They suggested that this asymmetry was consistent with a "tangential friction" model. A recent neutron-projectilelike fragment coincidence study[39] showed an asymmetry of preequilibrium neutrons in peripheral collisions of $^{12}C + ^{158}Gd$ at 16 MeV/nucleon. The enhancement was on the side opposite the detected fragment, just as we observe, but opposite to that of Refs. 16 and 17. Clearly, more coincidence studies of preequilibrium particle emission are necessary before we can unravel the dynamics of the early stages of the nuclear collision mechanism.

We find it useful to define an "asymmetry parameter" as the transverse component of the IRS velocity: $(V_{\rm IRS})\sin\theta_{\rm IRS}$. The asymmetry is strongest for fragments at 10° for the Ho target, so this is the case we choose to study further. Shown in Fig. 20 is a plot of $(V_{\rm IRS})\sin\theta_{\rm IRS}$ vs $Z_{\rm LF}$. We see that the value of the asymmetry parameter is nonzero only for collisions which lead to high energy fragments, i.e., only for peripheral collisions. Also, the asymmetry tends to increase with the size of the detected fragment. If one adopts the simple picture that in peripheral interactions the transverse momentum of the fragment is balanced mainly by that of the IRS, then the variation of the asymmetry parameter with $A_{\rm LF}$, and hence with $Z_{\rm LF}$, can easily be understood. In peripheral collisions leading to high energy carbon fragments, for example, only a few nucleons in the initial projectile-target overlap region participate in transverse momentum conservation. Therefore, the average velocity of the localized interaction region must be strongly directed to the side opposite the detected fragment. At the other extreme, where we detect lithium fragments, the number of nucleons contained in the initial overlap region is greater. Hence, the velocity required for a given momentum is less. Also, since $A_{\rm LF}$ is smaller, the amount of transverse momentum of the fragment needing to be balanced is less. So this "larger" localized region (IRS) can move more slowly to the side opposite. In collisions giving rise to low energy fragments there is larger kinetic energy loss, indicating a longer interaction time.[29] Therefore, one might reasonably expect there to be more interaction between the projectile and the mean field of the target nucleus, meaning that the target nucleus would participate more in balancing the momentum of the fragment. In this case, the direction of the IRS would not have to be correlated strongly with the direction of the fragment, and the IRS could then move on the average straight down the beam axis, i.e., with asymmetry parameter equal to zero.

The above discussion for peripheral collisions suggests a method for crudely estimating an average size of the localized region of randomization, viz., $A_{\rm IRS}$, the number of nucleons in the IRS. Neglecting the contribution of the TLS, the momentum of the nitrogen projectile, $P_{\rm N}$, is taken up by the IRS and the LF. Hence,

$$P_{\rm IRS}^2 = P_{\rm N}^2 + P_{\rm LF}^2 - 2P_{\rm N}P_{\rm LF}\cos\theta_{\rm LF} . \quad (4)$$

Therefore,

$$2A_{\rm IRS}^2(E/A)_{\rm IRS} = 2\cdot 14\cdot 490 + 2A_{\rm LF}E_{\rm LF} - 4[(14\cdot 490)(A_{\rm LF}E_{\rm LF})]^{1/2}\cos\theta_{\rm LF} .$$

This equation is applied only where the reaction is expected to be peripheral, i.e., for HE fragments at angles near the grazing angle (7° for the Ni target and 7° and 10° for the Ho target). To obtain $A_{\rm IRS}$ from this equation a fragment angle and a species (Li, Be, B, or C) are chosen, and average values are used for the fragment mass number and energy. The average values are obtained from Figs. 2, 4, and 5 and from figures similar to Fig. 2, but for Ni and Ho at 7°. The values of $(E/A)_{\rm IRS}$ used are those shown in Fig. 18.

The results are given in Table III. $A_{\rm IRS}$ seems to be nearly independent of the target nucleus. For each set of data the IRS gets smaller as the fragment gets larger. This suggests a mechanism whereby the ^{14}N projectile emits a fragment and the remainder of the 14 nucleons enter the target to form an IRS. In a simple-minded approach the IRS, whose velocity is about half the beam velocity, would be composed of equal numbers of projectile and target nucleons. The IRS would then consist of $2(14 - A_{\rm LF})$ nucleons. This quantity is also given in the fourth column of Table III, and the agreement between the two methods is very good. This agreement is further evidence that the preequilibrium neutrons are emitted after perhaps only a single projectile nucleon-target nucleon collision.

For central collisions neglect of the TLS momentum is not valid, and the above method cannot be used to esti-

TABLE III. Mass number of IRS in peripheral collisions. $A_{\rm LF}$ is the average mass number of the detected fragment. $A_{\rm IRS}$ is computed from the data.

	Target=Ni, fragment angle=7°		
LF	$A_{\rm LF}$	$A_{\rm IRS}$	$2(14-A_{\rm LF})$
Li	6.5	14.2	15.0
Be	7.8	11.9	12.4
B	10.5	7.4	7.0
C	12.0	5.2	4.0
	Target=Ho, fragment angle=7°		
LF	$A_{\rm LF}$	$A_{\rm IRS}$	$2(14-A_{\rm LF})$
Li	6.7	20.8	14.6
Be	8.6	13.5	10.8
B	10.7	8.0	6.6
C	12.0	5.1	4.0
	Target=Ho, fragment angle=10°		
LF	$A_{\rm LF}$	$A_{\rm IRS}$	$2(14-A_{\rm LF})$
Li	6.8	14.5	14.4
Be	8.2	14.2	11.6
B	10.5	8.9	7.0
C	12.0	6.4	4.0

mate an IRS mass number. Instead, we use conservation of energy to obtain limits on this quantity. One assumption we can make is that the projectile enters the target nucleus and the projectile energy, 490 MeV, is shared directly between the IRS and the TLS. All other light particles, such as neutrons, protons, and fragments, get their energy from these two sources and come out later. If we use E to represent the total of kinetic and excitation energy, the assumption is

$$E_{\mathrm{IRS}}+E_{\mathrm{TLS}}=490\ \mathrm{MeV}\ . \tag{5}$$

But if the TLS gets its energy (subsequently) from the IRS, we should instead write

$$E_{\mathrm{IRS}}=490\ \mathrm{MeV}\ . \tag{6}$$

Thus the limits are given by

$$490\ \mathrm{MeV}-E_{\mathrm{TLS}}\leq E_{\mathrm{IRS}}\leq 490\ \mathrm{MeV}\ , \tag{7}$$

with the actual value depending on how much energy goes into making the TLS at the start of the collision. If we assume that the energy of each source is of the form $A(E/A)+A\tau^2/8$, then Eq. (7) gives bounds for A_{IRS} that can be determined from the E/A and τ fit parameters, with the assumption that $A_{\mathrm{TLS}}\approx A_{\mathrm{target}}$. These bounds are listed in Table IV for the cases that might best be expected to result from a central collision, viz., for the largest fragment angle for each target and with the LE fragment gate. The values for Ni suggest that perhaps not all of the 14 nucleons of the projectile become part of the IRS. We also see that, unlike the peripheral collisions, in the more central collisions there is no monotonic dependence of A_{IRS} on the mass of the detected fragment. Indeed, when the target is Ni there is no dependence on fragment mass.

In a study of preequilibrium neutron emission in the C + Gd and Ne + Gd systems at 4–11 MeV/nucleon above the Coulomb barrier, Gavron *et al.*[34] have also considered the size, or more appropriately, the composition of the IRS. Based on the source velocity deduced for central collisions they found that each projectile nucleon in the "hot spot" had interacted with approximately three target nucleons. Our values of E/A_{IRS} (Fig. 18) for central collisions are near the value corresponding to the nucleon-nucleon center-of-mass velocity, i.e., about 8 MeV, indicting that preequilibrium neutrons are emitted after projectile nucleons have interacted on the average with only one target nucleon.

Finally, the measured IRS multiplicity is plotted versus fragment angle in Fig. 21. It does seem significant that the same behavior observed for the TLS multiplicities is also evident here: (1) M_{IRS} increases with fragment angle; (2) M_{IRS} is larger for the low energy fragment gate than for the high energy gate; (3) M_{IRS} for the Ho target is larger than for the corresponding cases with the Ni target. The fact that the multiplicities of both sources exhibit the same behavior with angle and energy of the fragment and with target mass suggests that there is a very intimate relation between the IRS and the TLS. We feel this is a further indication that the neutrons parametrized by the IRS emerge very early in the interaction from a "hot" subset of the "cooler" targetlike fragment nuclear matter (consistent with conclusions drawn from charged particle work).[20,23,25]

Having discussed the IRS parameters we now return to the "missing-momentum" plot in Fig. 14. We have observed extensive preequilibrium neutron emission which we parametrized with an IRS. Could the IRS explain the missing momentum? It is noteworthy that the missing

TABLE IV. Lower and upper limits on A_{IRS} in central collisions.

Fragment	Ni—23°	Ho—30°
Li	11–16	18–28
Be	11–14	17–26
B	9–12	33–42
C	11–16	35–45

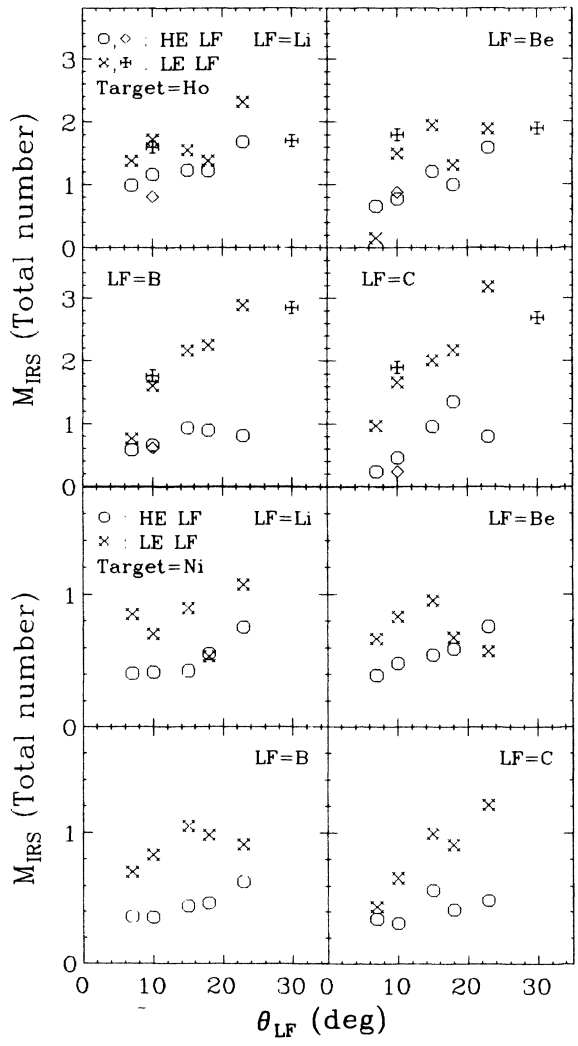

FIG. 21. The IRS multiplicity, M_{IRS}, vs fragment angle. The format is the same as that of Fig. 11. (Note the difference in scale between the Ho and Ni data.)

momentum observed (Fig. 14) is largest for strongly damped reactions. These reactions are also where the IRS multiplicity is largest. But it is equally noteworthy that at small θ_{LF}, where $P_{missing}$ is maximum, is precisely where the IRS multiplicity is a minimum. Ascribing the missing momentum to the IRS, then, is consistent with the dependence of $P_{missing}$ on the energy damping of the interaction, but not with its dependence on θ_{LF}. At small θ_{LF} some additional mechanism is necessary to account for $P_{missing}$, and two likely candidates are projectile fragmentation (both prompt and delayed[59]) and LF sequential decay. We detect neutrons in coincidence with a single LF. But if the detected LF were the result of projectile fragmentation, then the momentum carried by the undetected piece would be "missing" from our analysis. In a similar fashion, if a substantial fraction of the LF had undergone sequential decay prior to detection, then the momentum carried by the emitted particles would be "missing." In a recent study of transfer and breakup processes in reactions of Ne + Au,[60] two striking observations were made concerning the fraction of inclusive fragment yield that had participated in sequential decay prior to detection. (1) This fraction was largest for the smallest LF. (2) This fraction appeared to be increasing with beam energy, resulting in values of 0.4 and 0.7 for beam energies of 11 and 17 MeV/nucleon, respectively. This suggests that at 35 MeV/nucleon a large fraction of the inclusive fragment yield is the by-product of sequential decay, making this a possible source of the missing momentum.

VI. SUMMARY AND CONCLUSIONS

We have compiled an extensive set of neutron-fragment coincidence data for the $^{14}N + {}^{165}Ho$ and $^{14}N + Ni$ systems at 35 MeV/nucleon. The fragment energy and angular distributions show a rather clear division into quasielastic processes leading to high energy fragments and strongly damped reactions leading to low energy fragments. To gain insight into the differences in their respective reaction mechanisms, we set gates across high energy and low energy fragments and examined the coincident neutron spectra. The neutron spectra consisted of three components: the projectilelike fragment and TLS components, and a preequilibrium component ascribed to an IRS. For the present work we neglected the projectilelike fragment contribution and focused on the TLS and IRS components. Each source was described by a temperature, kinetic energy per nucleon, direction, and a multiplicity, as determined by fitting the neutron spectra.

The fit parameters describing the TLS were compared with a two-body kinematics calculation, with the observation that there was considerable missing momentum in the forward direction, especially for highly damped collisions. We have concluded that a significant part of the missing momentum is due to preequilibrium particle emission. But the angular dependence of the missing momentum suggests that projectile fragmentation or sequential decay are also contributing appreciably, especially at small fragment angle.

The TLS temperature is about 2.5 MeV for the Ho target and about 3.5 MeV for the Ni target. In spite of the fact that the TLS temperature is independent of fragment angle, the number of TLS neutrons per fragment increases with fragment angle. Comparison of this measured TLS multiplicity with predictions from the statistical code CASCADE indicates that many collisions resulting in a detected fragment do not excite the target fragment to energies above the neutron emission threshold. This is especially true for peripheral collisions, suggesting a strong angular dependence of the competition between transfer reactions and projectile breakup.

The velocity of the IRS, about one-half the projectile velocity, is an order of magnitude greater than the velocity of the TLS. In peripheral collisions the IRS is directed to the side of the beam opposite the coincident fragment, and its high speed then reproduces a left-right asymmetry of its emitted neutrons, in agreement with observation. The neutron multiplicity of the IRS is about $\frac{1}{4}$ the multiplicity of the TLS. The temperature of the IRS is about 8.5 MeV when the target is Ho and about 10 MeV when it is Ni.

The size of the IRS was estimated in peripheral collisions by assuming that the momentum of the projectile is balanced after the collision by the fragment and the IRS. The results are the same for both targets and vary steadily from about 14 for the lightest detected fragment (Li) to about 5 for the heaviest (C). In central collisions energy conservation is used to put lower and upper limits on the size of the IRS. When the target is Ni all four fragment species (Li, Be, B, C) are associated with the same IRS mass limits, about 10–15 mass units, and perhaps not all of the 14 projectile nucleons participate with target nucleons in forming an IRS. When the target is Ho the values are much larger, perhaps 20 to 40.

Examination of the IRS fit parameters show that neither the IRS temperature nor its velocity exhibits a clear trend with fragment energy or angle. We interpret this as an indication that preequilibrium neutrons are emitted in the very early stages of the interaction before the "final fate" of the fragment has been determined. The IRS may be an evolving localization of high excitation energy with neutrons emitted early after its formation when the IRS is "hot and small," perhaps after participating projectile nucleons have undergone as few as 1–2 collisions. If composite particles are also emitted from the IRS, this emission occurs later in the evolution of the IRS after it has become "larger and cooler." Our analysis has not addressed the question of spatial localization of the IRS, though, and "large" and "small" refer only to the average number of nucleons participating in the IRS.

ACKNOWLEDGEMENTS

We acknowledge the efforts of the Operations Group at the National Superconducting Cyclotron Laboratory (NSCL). We would also like to thank Dr. D. Hilscher for his encouragement and many helpful discussions. This material is based on work supported by the National Science Foundation under Grants. No. PHY 83-12245, INT-80-15333, and PHY 84-16025 and by the Hungarian Academy of Sciences.

*Present address: Lawrence Livermore National Laboratory, Livermore, CA 94550.

†Present address: Donnelly Corp, Holland, MI 49423.

[1]C. K. Gelbke, C. Olmer, M. Buenerd, D. L. Hendrie, J. Mahoney, M. C. Mermaz, and D. K. Scott, Phys. Rep. **42**, 311 (1978).

[2]F. Pühlhofer, Nucl. Phys. **A280**, 267 (1977).

[3]J. Negele, Rev. Mod. Phys. **54**, 913 (1982).

[4]G. D. Westfall, J. Gosset, P. J. Johansen, A. M. Poskanzer, W. G. Meyer, H. H. Gutbrod, A. Sandoval, and R. Stock, Phys. Rev. Lett. **37**, 1202 (1976).

[5]J. Cugnon, Phys. Rev. C **22**, 1885 (1980).

[6]J. Aichelin and G. Bertsch, Phys. Rev. C **31**, 1730 (1985).

[7]M. Blann, Phys. Rev. C **31**, 1245 (1985).

[8]J. P. Bondorf, J. N. De, G. Fai, A. O. Karvinen, B. Jakobsson, and J. Randrup, Nucl. Phys. **A333**, 285 (1980).

[9]S. Leray, G. La Rana, and C. Ngo, Z. Phys. A **320**, 383 (1985).

[10]W. W. Morison, S. K. Samaddar, D. Sperber, and M. Zielinska-Pfabe, Phys. Lett. **93B**, 379 (1980).

[11]R. Weiner and M. Weström, Nucl. Phys. **A286**, 282 (1977).

[12]J. J. Griffin, Phys. Lett. **24B**, 5 (1967).

[13]M. Blann, Annu. Rev. Nucl. Sci. **25**, 123 (1975).

[14]G. Mantzouranis, H. A. Weidenmüller, and D. Agassi, Z. Phys. A **276**, 145 (1976).

[15]D. H. E. Gross and J. Wilczynski, Phys. Lett. **67B**, 1 (1977).

[16]C. K. Gelbke, M. Bini, C. Olmer, D. L. Hendrie, J. L. Laville, J. Mahoney, M. C. Mermaz, D. K. Scott, and H. H. Wieman, Phys. Lett. **71B**, 83 (1977).

[17]I. Tserruya, A. Breskin, R. Checkik, A. Fraenkel, S. Wald, N. Zwang, R. Bock, M. Dakowski, A. Gobbi, H. Sann, R. Bass, G. Kreyling, R. Renfordt, K. Stelzer, and U. Arlt, Phys. Rev. C **26**, 2509 (1982).

[18]G. D. Harp, J. M. Miller, and B. J. Berne, Phys. Rev. **165**, 1166 (1968).

[19]T. C. Awes, G. Poggi, S. Saini, C. K. Gelbke, R. Legrain, and G. D. Westfall, Phys. Lett. **103B**, 417 (1981).

[20]T. C. Awes, S. Saini, G. Poggi, C. K. Gelbke, D. Cha, R. Legrain, and G. D. Westfall, Phys. Rev. C **25**, 2361 (1982).

[21]B. V. Jacak, G. D. Westfall, C. K. Gelbke, L. H. Harwood, W. G. Lynch, D. K. Scott, H. Stöcker, and M. B. Tsang, Phys. Rev. Lett. **51**, 1846 (1983).

[22]G. D. Westfall, Z. M. Koenig, B. V. Jacak, L. H. Harwood, G. M. Crawley, M. W. Curtin, C. K. Gelbke, B. Hasselquist, W. G. Lynch, A. D. Panagiotou, D. K. Scott, H. Stöcker, and M. B. Tsang, Phys. Rev. C **29**, 861 (1984).

[23]D. J. Fields, W. G. Lynch, C. B. Chitwood, C. K. Gelbke, M. B. Tsang, H. Utsunomiya, and J. Aichelin, Phys. Rev. C **30**, 1912 (1984).

[24]B. B. Back, K. L. Wolf, A. C. Mignerey, C. K. Gelbke, T. C. Awes, H. Breuer, V. E. Viola, Jr., and P. Dyer, Phys. Rev. C **22**, 1927 (1980).

[25]T. C. Awes, G. Poggi, C. K. Gelbke, B. B. Back, B. G. Glagola, H. Breuer, and V. E. Viola, Jr., Phys. Rev. C **24**, 89 (1981).

[26]M. B. Tsang, C. B. Chitwood, D. J. Fields, C. K. Gelbke, D. R. Klesch, W. G. Lynch, K. Kwiatkowski, and V. E. Viola, Jr., Phys. Rev. Lett. **52**, 1967 (1984).

[27]G. R. Young, R. L. Ferguson, A. Gavron, D. C. Hensley, Felix E. Obenshain, F. Plasil, A. H. Snell, M. P. Webb, G. F. Maguire, and G. A. Petitt, Phys. Rev. Lett. **45**, 1389 (1980).

[28]B. E. Hasselquist, G. M. Crawley, B. V. Jacak, Z. M. Koenig, G. D. Westfall, J. E. Yurkon, R. S. Tickle, J. P. Dufour, and T. J. M. Symons, Phys. Rev. C **32**, 145 (1985).

[29]D. Hilscher, E. Holub, U. Jahnke, H. Orf, and H. Rossner, in *Dynamics of Heavy-Ion Collisions,* edited by N. Cindro, R. A. Ricci, and W. Greiner (North-Holland, Amsterdam, 1981).

[30]D. Hilscher, E. Holub, G. Ingold, U. Jahnke, H. Orf, and H. Rossner, Lecture presented by D. Hilscher at the XV Masurian Summer School on Nuclar Reactions, Mikolajke, Poland, 1983.

[31]E. Holub, D. Hilscher, G. Ingold, U. Jahnke, H. Orf, and H. Rossner, Phys. Rev. C **28**, 252 (1983).

[32]D. Hilscher, E. Holub, G. Ingold, U. Jahnke, H. Orf, H. Rossner, W. U. Schröder, H. Gemmeke, K. Keller, L. Lassen, and W. Lücking, in *Conference Proceedings from the Workshop on Coincidence Particle Emission from Continuum States at Bad Honnef, 1984* (World Scientific, Singapore, 1984), p. 268.

[33]A. Gavron, J. R. Beene, R. L. Ferguson, F. E. Obenshain, F. Plasil, G. R. Young, G. A. Petitt, K. Geoffroy Young, M. Jääskeläinen, D. G. Sarantites, and C. F. Maguire, Phys. Rev. C **24**, 2048 (1981).

[34]A. Gavron, J. R. Beene, B. Cheynis, R. L. Ferguson, F. E. Obenshain, F. Plasil, G. R. Young, G. A. Pettit, C. F. Maguire, D. G. Sarantites, M. Jääskeläinen, and K. Geoffroy-Young, Phys. Rev. C **27**, 450 (1983).

[35]J. Kasagi, S. Saini, T. C. Awes, A. Galonsky, C. K. Gelbke, G. Poggi, D. K. Scott, K. L. Wolf, and R. L. Legrain, Phys. Lett. **104B**, 434 (1981).

[36]D. Hilscher, J. R. Birkelund, A. D. Hoover, W. U. Schröder, W. Wilcke, J. R. Huizenga, A. C. Mignerey, K. L. Wolf, H. F. Breuer, and V. E. Viola, Jr., Phys. Rev. C **20**, 576 (1979).

[37]H. Gemmeke, P. Netter, Ax. Richter, L. Lassen, S. Lewandowski, W. Lücking, and R. Schreck, Phys. Lett. **97B**, 213 (1980).

[38]G. Caskey, A. Galonsky, B. Remington, M. B. Tsang, C. K. Gelbke, A. Kiss, F. Deak, Z. Seres, J. J. Kolata, J. Hinnefeld, and J. Kasagi, Phys. Rev. C **31**, 1597 (1985).

[39]G. A. Petitt, A. Gavron, J. R. Beene, B. Cheynis, R. L. Ferguson, F. E. Obenshain, F. Plasil, G. R. Young, M. Jääskeläinen, D. G. Sarantites, and C. F. Maguire, Phys. Rev. C **32**, 1572 (1985).

[40]W. Lücking, R. Schreck, K. Keller, L. Lassen, A. Nagel, and G. Gemmeke, Z. Phys. A **320**, 585 (1985).

[41]B. Chambon, D. Drain, C. Pastor, A. Dauchy, A. Giorni, and C. Morand, Z. Phys. A **312**, 125 (1983).

[42]B. A. Remington, G. Caskey, A. Galonsky, C. K. Gelbke, M. B. Tsang, Z. Seres, F. Deak, A. Kiss, J. Kasagi, and J. J. Kolata, in *Proceedings of the 4th International Conference on Nuclear Reaction Mechanisms, Varenna, Italy,* edited by E. Gadioli (University of Milan, Milan, 1985) (Ricerca Scientifica Educazione Permanente, Supplemento No. 46, 1985, p. 161).

[43]A. Kiss, F. Deak, Z. Seres, G. Caskey, A. Galonsky, L. Heilbronn, B. Remington, and J. Kasagi, submitted to Phys. Lett.

[44]F. Deak, A. Kiss, Z. Seres, G. Caskey, A. Galonsky, B. Remington, C. Gelbke, B. Tsang, and J. J. Kolata, submitted to Nucl. Phys.

[45]B. A. Remington, Ph.D. thesis, Michigan State University, 1986.

[46]P. Sperr, H. Speier, M. R. Maier, and D. Evers, Nucl. Instrum. Methods **116**, 55 (1974).

[47]R. St. Onge, A. Galonsky, R. K. Jolly, and T. M. Amos, Nucl. Instrum. Methods **126**, 391 (1975).

[48]L. J. Perkins and M. C. Scott, Nucl. Instrum. Methods **166**, 451 (1979).

[49]A. Vander Molen, R. Au, R. Fox, and T. Glynn, Nucl. Instrum. Methods **A236**, 359 (1985).

[50]W. A. Friedman, Phys. Rev. C **27**, 569 (1983).

[51]G. J. Wozniak, N. A. Jelley, and Joseph Cerney, Nucl. In-

strum. Methods **120**, 29 (1974).

[52]R. A. Cecil, B. D. Anderson, and R. Madey, Nucl. Instrum. Methods **161**, 439 (1979).

[53]R. J. Kurz, University of California Radiation Lab Internal Report UCRL-11339, 1964.

[54]C. K. Gelbke, in *Proceedings of the International Symposium on Continuum Spectra of Heavy Ion Reactions held in San Antonio, Texas,* edited by T. Tamura, J. B. Natowitz, and D. H. Youngblood (Harwood-Academic, New York, 1979).

[55]G. Caskey, A. Galonsky, B. Remington, F. Deak, A. Kiss, and Z. Seres, Phys. Rev. C **34**, 506 (1986).

[56]K. J. Le Couteur and D. W. Lang, Nucl. Phys. **13**, 32 (1959).

[57]P. Dyer, T. C. Awes, C. K. Gelbke, B. B. Back, A. Mignerey, K. L. Wolf, H. Breuer, V. E. Viola, Jr., and W. G. Meyer, Phys. Rev. Lett. **42**, 560 (1979).

[58]U. Jahnke, G. Ingold, H. Homeyer, M. Bürgel, Ch. Egelhaaf, H. Fuchs, and D. Hilscher, Phys. Rev. Lett. **50**, 1246 (1983).

[59]W. A. Friedman and D. Saloner, Phys. Rev. C **23**, 2532 (1981).

[60]S. Wald, S. B. Ganzes, C. R. Albiston, Y. Chan, B. G. Harvey, M. J. Murphy, I. Tserruya, R. G. Stokstad, P. J. Countryman, K. Van Bibber, and H. Homeyer, Phys. Rev. C **32**, 894 (1985).